2-D Geodynamic Modeling of the Central South Atlantic Wide Rifted Margins, Implications for Evaporite Deposition

T Theunissen, R S Huismans, D Rouby, C Gout

JGR Solid Earth

RESEARCH ARTICLE
10.1029/2023JB027985

2-D Geodynamic Modeling of the Central South Atlantic Wide Rifted Margins, Implications for Evaporite Deposition

T. Theunissen[1], R. S. Huismans[1], D. Rouby[2], and C. Gout[3,4]

[1]Department of Earth Science, University of Bergen, Bergen, Norway, [2]Observatoire Midi-Pyrénées, Université Toulouse 3, GET, UMR 5563, Toulouse, France, [3]TotalEnergies SE, Centre Scientifique et Technique Jean-Feger, Pau, France, [4]E2S, LFCR, Université de Pau de des Pays de l'Adour, Pau, France

Key Points:

- Weak lower crust and syn-rift sedimentation rate are first-order controls on the formation and geometry of wide distal rifted margin
- Modeling suggests a base level ∼−600 m below present-day global sea level (bsl) during the distal margin formation before evaporite deposition
- Modeling suggests a base level of ∼−300/−400 m bsl at the end of evaporite deposition

Supporting Information:

Supporting Information may be found in the online version of this article.

Correspondence to:

T. Theunissen,
thomas.theunissen@uib.no

Citation:

Theunissen, T., Huismans, R. S., Rouby, D., & Gout, C. (2024). 2-D geodynamic modeling of the Central South Atlantic wide rifted margins, implications for evaporite deposition. *Journal of Geophysical Research: Solid Earth*, *129*, e2023JB027985. https://doi.org/10.1029/2023JB027985

Received 1 OCT 2023
Accepted 19 APR 2024

Author Contributions:

Conceptualization: T. Theunissen, R. S. Huismans, D. Rouby
Funding acquisition: R. S. Huismans
Investigation: T. Theunissen
Methodology: T. Theunissen, R. S. Huismans, D. Rouby
Project administration: R. S. Huismans, C. Gout
Resources: R. S. Huismans, C. Gout
Validation: D. Rouby, C. Gout
Writing – original draft: T. Theunissen
Writing – review & editing: T. Theunissen, R. S. Huismans, D. Rouby, C. Gout

Abstract The thick late syn- to early post-rift shallow water evaporites in the most distal part of wide rifted margins is paradoxical with the deep depression at crustal breakup time predicted by isostatically compensated lithospheric thinning. Elevation of the distal margin and water depth during deposition of the late syn-rift evaporites in the central South Atlantic are not well constrained and remain to be quantified. We use forward 2-D thermo-mechanical modeling coupled with melt prediction and surface processes to assess the contribution of lithospheric and mantle processes on the distal margin topography and subsidence history during continental rifting. Models show that (a) counter-flow of depleted lower lithospheric mantle during rifting explains the magma-poor nature of these margins and (b) weak crust and syn-rift sediment control the wide crustal necking and subsidence history of the distal margin. Integration of our modeling results with quantified geophysical and geological observations suggests that (a) base level was down to −600 m below present-day global sea level (bsl) during distal margin formation in the Aptian before sag and evaporite deposition, (b) base level was about −300/−400 m bsl at the end of evaporite deposition, and (c) scenarios with a fixed shallow base level (−400 m bsl) or with an increasing base level from an initially deep position (−1,600 m bsl) during evaporite deposition can both fit the observed evaporite distribution. However, erosional features along the base of evaporites suggest a deep initial base level.

Plain Language Summary The opening of the Atlantic Ocean contributed to the fragmentation of the Pangaea supercontinent 100–200 millions years ago. Water depth in the basins formed during this process is not well constrained while it is fundamental to understand their environmental conditions. For instance, in the central South Atlantic that comprises the west African Gabon, Congo, and Angola margins and their conjugates along the Brazilian margin, a giant evaporite basin deposited during continental breakup in shallow water formed very far from the continent. In this study, we compiled data along these margins and used 2-D numerical models to show that an initially deep basin isolated from global ocean can provide the conditions necessary for this giant evaporite basin to be deposited.

1. Introduction

The wide rifted margins of the central South Atlantic exhibit a giant evaporite basin that extends from onshore to the distal margin next to the oceanic crust and from the Ascension fracture zone in the north and the Rio Grande fracture zone in the south (Figure 1) (e.g., Brognon & Verrier, 1966; Karner & Gambôa, 2007; Kukla et al., 2018; Moulin et al., 2010; Pichel et al., 2023). The conjugate margins formed during breakup of the Pangaea supercontinent in the Early Cretaceous (∼145–115 Ma) (e.g., R. Guiraud & Maurin, 1991) and a very thick evaporite basin formed during the late syn-rift and early post-rift (e.g., Karner & Gambôa, 2007). Evaporites usually form by evaporation of sea water under very shallow marine (0–100 m) and arid climate conditions (e.g., Warren, 2016, and references therein). The presence of large amounts of evaporites in the distal margin suggest that its elevation was close to global sea level at crustal breakup time (e.g., Moulin et al., 2005; Reston, 2010; Watts & Ryan, 1976). This is, however, not compatible with the deep depression predicted by isostatically compensated lithospheric thinning during continental rifting (e.g., McKenzie, 1978; Steckler & Watts, 1978). The presence of evaporites in the distal margin remains therefore paradoxical in terms of geodynamic context.

Two classes of mechanisms have been proposed to explain the geodynamic conditions allowing evaporite deposition along the wide rifted margins of the central South Atlantic, both favoring an anomalously elevated distal margin during the late syn-rift close to global sea level. The first class considers a higher buoyancy of the

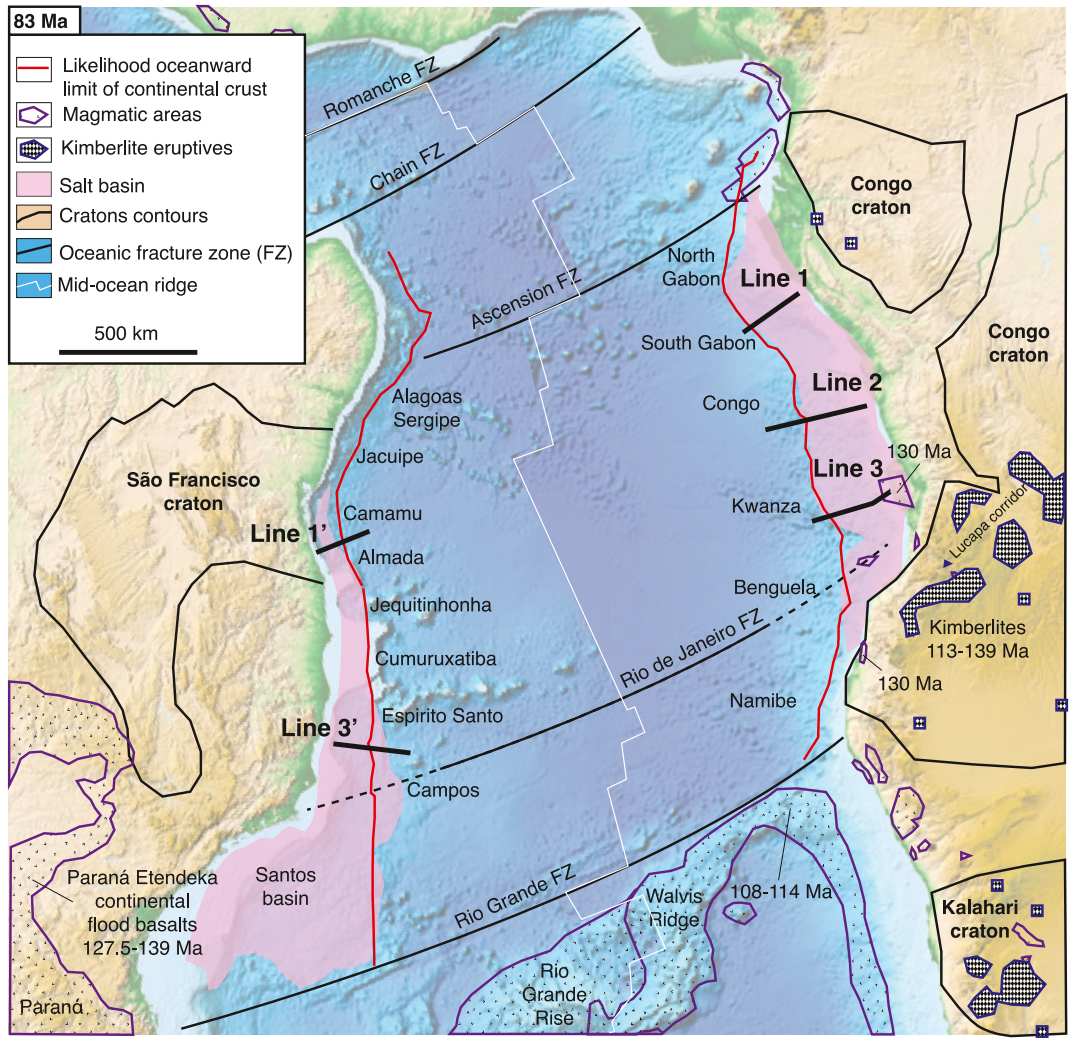

Figure 1. Reconstruction of the central South Atlantic at 83 Ma. Syn-rift and early post-rift magmatism are after Baksi (2018), Foulger (2018), Marsh and Swart (2018), Mohriak (2020), and Tappe et al. (2018). Oceanic fracture zones are after M. Guiraud et al. (2010). The map is build using GPlates (Müller et al., 2018), Mercator projection with meridian 0, African plate fixed, and plate boundaries and poles of rotation from Matthews et al. (2016) based on Heine et al. (2013).

distal margin's lithospheric column resulting from reduced average density. This encompasses depth-dependent lithospheric thinning (e.g., Davis & Kusznir, 2004; Dupre et al., 2007; Huismans & Beaumont, 2008; Royden & Keen, 1980), phase changes in the upper mantle (serpentinization, plagioclase-spinel-garnet stability fields) (e.g., Quirk & Ruepke, 2018; N. S. Simon & Podladchikov, 2008), thermal anomaly in the upper mantle (e.g., Pindell & Heyn, 2022), magmatic underplating (e.g., Quirk & Ruepke, 2018), or delayed crustal thinning after crustal breakup (e.g., Aslanian et al., 2009; Moulin et al., 2005; Pindell et al., 2014). The second class considers dynamic support from the convective upper mantle with varying densities (e.g., Beniest et al., 2017; Blaich et al., 2011; Crosby et al., 2011). Each of these mechanisms may produce a shallower late syn-rift distal margin. However, phase changes cannot explain enough uplift in the distal margin to raise it close to global sea level (e.g., Quirk & Ruepke, 2018), a thermal anomaly and mantle melting in the upper-mantle beneath the distal margin (depth-dependent thinning, magmatic underplating) are incompatible with the magma-poor nature of most of the central South Atlantic (Aslanian et al., 2009; Contrucci et al., 2004), and there are no clear mechanisms for a delayed crustal thinning after crustal breakup or for a regional dynamic support in the rift of the central South Atlantic (Aslanian et al., 2009; Crosby et al., 2011; Pindell et al., 2014). Other studies proposed that evaporites were deposited at global sea level only in the proximal domain of the rifted margin and then flowed toward the deep distal margin (e.g., Cowie et al., 2016; Davison et al., 2012). Alternatively, a low base level in a distal basin

isolated from the global sea could explain both the shallow water environment during evaporite deposition and the significant late syn-rift accommodation during marine transgression (Crosby et al., 2011; Davison et al., 2012; Karner & Gambôa, 2007; Montaron & Tapponier, 2010; Nunn & Harris, 2007; Reston, 2009, 2010; Rowan, 2014, 2022). It has indeed been suggested that the basin has been isolated from global sea water circulation by a barrier formed by the Walvis volcanic ridge and by the Rio Grande Rise in the South from the Berriasian to the Albian-Cenomanian (Figure 1) (e.g., Burke & Sengör, 1988; Burke et al., 2003; Cui et al., 2023; Dingle, 1999; Jackson et al., 2000; Karner & Gambôa, 2007; Szatmari, 2000). The absolute elevation of the distal margin in the central South Atlantic and the associated water depth during syn-rift and early post-rift remain nonetheless to be quantified.

In this work, we use 2-D forward geodynamic modeling to understand the rheological and thermal conditions of the lithosphere that allow reproducing characteristics of the central South Atlantic rifted margins such as the total extension, crustal thickness, width of distal margins, syn-rift sediment thickness, and magmatic budget. We aim to predict the absolute elevation of the distal rifted margin at the time of evaporite deposition, that is, close to lithospheric breakup time. The forward 2-D thermo-mechanical models, coupled with melt prediction and surface processes, allow self-consistent assessment of the contribution of lithospheric and mantle processes, and of sediment load on topography. We first review the state of the art on lithospheric, crustal, and stratigraphic architecture of the central South Atlantic rifted margins. We then present the compiled data to assess along strike variations of crustal structure and sediment thicknesses. We summarize the methodology and the model setup, and describe eight models selected for comparison with these observations. We use these models to assess the conditions of deposition of late syn-rift sag sediments, evaporites, and early post-rift carbonates and discuss the implications of models for the central South Atlantic in terms of base level evolution during and just after rifting.

2. Geological Setting

The study area includes the South Gabon to South Kwanza (North Angola) basins and Camamu to Espirito Santo basins (Brazil) respectively on the West African and on South American rifted margins (Figures 1 and 2a).

2.1. Plate Kinematic Constraints on Rifting and Breakup Timing

Recent plate reconstructions suggest that South Atlantic rifting occurred in two phases: a first phase of moderately oblique extension (145–125 Ma) followed by a second phase of orthogonal extension (125–115 Ma) (Brune et al., 2016; Heine et al., 2013; Matthews et al., 2016) (Figure 2). The age and position of crustal breakup are not very well constrained (Blaich et al., 2011; Norton et al., 2016). Indeed, plate reconstruction are associated with uncertainties resulting from the integration of deformation inside the African and South American plates (Moulin et al., 2010; Seton et al., 2012; Torsvik et al., 2009). In addition, breakup took place during the Cretaceous normal polarity superchron resulting in limited constraints from magnetic anomalies on the age of the first oceanic crust (Moulin et al., 2010; Seton et al., 2012; Torsvik et al., 2009). Furthermore, the transition area from the last unequivocal continental crust to oceanic crust is locally relatively wide as a consequence of unconstrained interpretations of seismic data (Loureiro et al., 2018; Norton et al., 2016; Romito & Mann, 2022; Torsvik et al., 2009). Despite these uncertainties, breakup time in the entire study area can be reasonably well constrained between 118 and 115 Ma (late Aptian) (Figure 2) (Matthews et al., 2016). Crustal breakup is concomitant with stabilization, after an acceleration, of the extension rate suggesting lithospheric breakup (Brune et al., 2016; Mueller et al., 2016) (Figure 2b). The kinematic reconstruction of Matthews et al. (2016) suggests that the total syn-rift extension is ∼300 km with an average extension rate of about 1 cm/year (30 Myr of extension) assuming crustal breakup at 115 Ma (Figure 2) (Heine et al., 2013; Matthews et al., 2016; Torsvik et al., 2009).

2.2. Rifted Margin Basin Stratigraphy

The evaporites of the central South Atlantic divide the sedimentary record into the pre-evaporite and post-evaporite megasequences (e.g., Asmus & Ponte, 1973; Campos et al., 1974; de Ruiter, 1979; Lehner & De Ruiter, 1977). The pre-evaporite megasequence corresponds to the syn-rift phase between the Berriasian and Aptian while the post-evaporite megasequence corresponds to the post-rift phase. The last phase of syn-rift deposition, called the "sag phase," and the deposition of evaporites record the transition from continental to a fully marine depositional environment. The sag phase and the evaporite deposition period form the "transition phase" whose deposits extend from the proximal to the distal margin with broadly parallel, mostly unfaulted

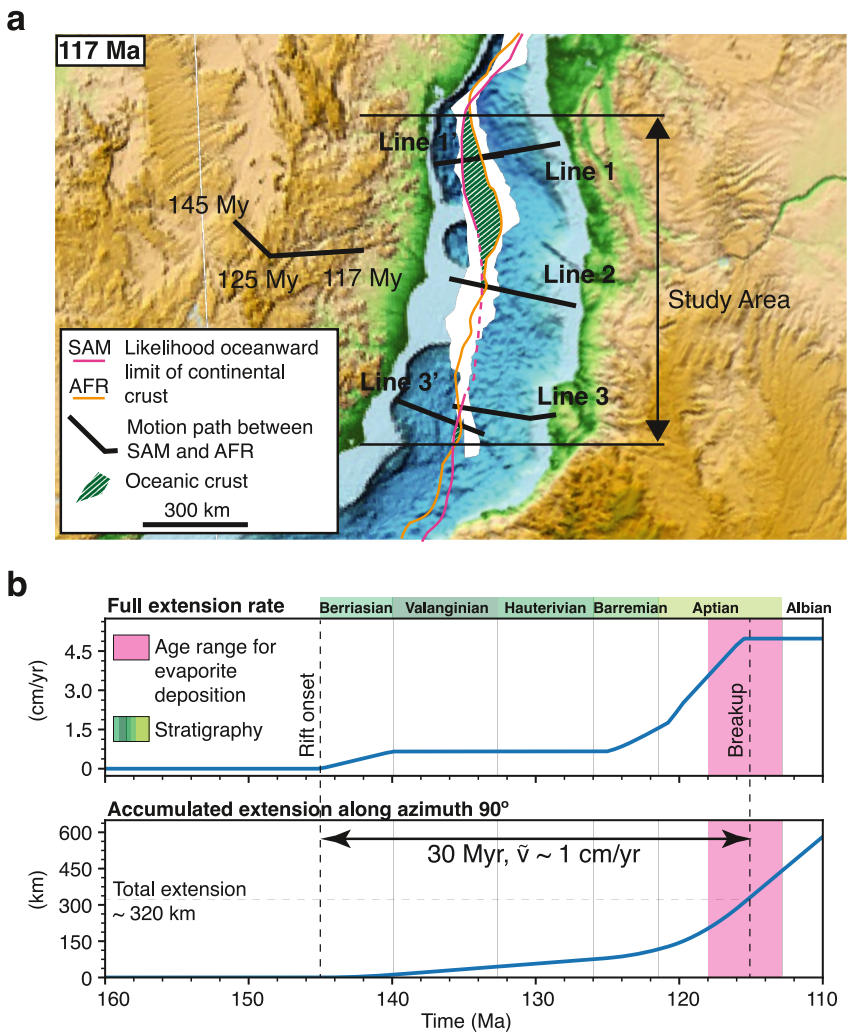

Figure 2. Early Cretaceous kinematics of the study area. (a) Reconstruction of the central South Atlantic around crustal breakup time (117 Ma) from poles of rotations and plate boundaries of Heine et al. (2013) and Matthews et al. (2016). (b) Corresponding full extension rate and total extension during rifting (GPlates; Müller et al., 2018). SAM, South America; AFR, Africa.

layers, except in the extreme distal margin (e.g., Beglinger et al., 2012b; Karner & Gambôa, 2007; Karner et al., 2003; Laspatzis et al., 2022; Moulin et al., 2005). The correlation of pre-evaporite strata is complicated by the lack of direct observations of their sedimentary facies and biostratigraphy in the distal margin (e.g., Anka et al., 2009; Laspatzis et al., 2022). Absolute ages used below are recalibrated using the latest chart of the International Commission on Stratigraphy (Cohen et al., 2013, 2023).

Early syn-rift deposits, from the Berriasian to Barremian (about 145 to 122 Ma), are mainly documented on tilted crustal blocks in the proximal domain. They record mostly continental depositional environments (alluvial fan, fluvial, lacustrine) (e.g., Beglinger et al., 2012a, 2012b; Behar et al., 2021; Cainelli & Mohriak, 1999; Chaboureau et al., 2013; Coward et al., 1999). The sag phase deposits (about 117 to 115 Ma) extend from the proximal to the distal margin (e.g., Karner et al., 2003; Moulin et al., 2005). They are unconformably overlying the early syn-rift deposits (e.g., Behar et al., 2021; Brownfield & Charpentier, 2006; Quirk et al., 2013). Onshore, the base of the sag corresponds to incised valleys, in the Congo, Kwanza, Benguela, and Namibe basins (Behar et al., 2021; Delhaye-Prat et al., 2016; Gindre-Chanu et al., 2016; Kebi-Tsoumou, 2018; Moragas et al., 2023; Van Eden, 1978). Offshore, some highs in Gabon record this erosional unconformity (e.g., Epin et al., 2021; Karner & Driscoll, 1999). This erosional unconformity corresponds, in the proximal margin, to a depositional hiatus in the Early Aptian (e.g., Behar et al., 2021; Chaboureau et al., 2013; Poropat & Colin, 2012; Thompson et al., 2015).

Sag deposits vary from thin sand-prone layer in the proximal domain to thicker lacustrine shales and marlstones toward the distal margin (e.g., Brownfield & Charpentier, 2006; Burwood, 1999; Karner et al., 2003; Marton et al., 2000; Saller et al., 2016). In the proximal margin of the Gabon, Kwanza, and Namibe basins, sag phase deposits evolve from conglomerates, sands, to lagoonal facies with increasing marine affinity (e.g., Bate et al., 2001; Karner & Gambôa, 2007; Moragas et al., 2023; Teisserenc & Villemin, 1989). The top of the sag unit is also an erosional unconformity that can be followed across the entire evaporite basin (Karner & Gambôa, 2007; Karner et al., 2003).

Evaporites were then deposited above this unconformity, during the late syn-rift to early post-rift over a period between 0.5 Ma and 5.5 Ma long (e.g., Azevedo et al., 2022; Davison et al., 2012; Eldrett et al., 2023; Karner & Gambôa, 2007; Rodriguez et al., 2018; Szatmari et al., 2021). Evaporite deposition may have started in the late Aptian between 116 and 113 Ma based on absolute ages of pre-evaporite volcanic rocks and carbonates (e.g., Azevedo et al., 2022; Lawson et al., 2022; Szatmari et al., 2021). However, a recent study pointed out that evaporite deposition in the proximal rifted margin in Gabon occurred during an interval straddling the Early-late Aptian boundary (~118.4–116.8 Ma) and that younger ages from absolute Ar/Ar dating might be corrupted by hydrothermal circulation (Eldrett et al., 2023). A 118–116 Ma age for evaporites is compatible with late syn-rift to early post-rift deposition in the kinematic reconstructions of Matthews et al. (2016). The proximal evaporites are generally characterized by layered sequences showing repetitive base level drop and flooding indicating shallow water conditions (Davison et al., 2012; Gindre-Chanu et al., 2022; Rodriguez et al., 2018).

Early post-evaporite deposits (Albian to Cenomanian) are mainly shallow water carbonates and distal mudstones (e.g., Marton et al., 2000; Rebelo et al., 2021; Séranne & Anka, 2005). After the Cenomanian, sedimentation evolved from carbonate- to more clastic-dominated and deeper depositional environments (Beglinger et al., 2012a; Coward et al., 1999; Laspatzis et al., 2022). Ostracods studies suggest that the Walvis ridge was not fully breached by global ocean circulation until Cenomanian-Turonian times and kept the central South Atlantic isolated before then (e.g., Bate, 1999; Dingle, 1996).

2.3. Syn-Rift Magmatism

The rifted margins of the central South Atlantic, in the study area, are magma-poor (e.g., Blaich et al., 2011; Contrucci et al., 2004; Epin et al., 2021; Moulin et al., 2005; Zalán et al., 2011). Only gravity modeling of the most distal part of the margins suggests intrusive magmatic rocks (Blaich et al., 2011; Fernandez et al., 2020). The nature of the transitional domain from continental to oceanic crust is not well constrained and has been interpreted as either proto-oceanic crust, exhumed mantle, lower continental crust, and/or continental crust intruded by magmatic rocks (Blaich et al., 2011; Epin et al., 2021; Fernandez et al., 2020; Loureiro et al., 2018; Péron-Pinvidic et al., 2015). In the South Kwanza basin, tholeiitic basalts are found locally in the proximal domain (Marzoli et al., 1999) (Figure 1). They represent the northernmost extent of the Paraná-Etendeka flood basalts at 135 Ma (Baksi, 2018), related to the Tristan da Cunha hotspot (e.g., Heine et al., 2013; Karner & Gambôa, 2007; Morgan, 1983).

2.4. Lithospheric Inheritance and Inherited Thermal State

The central South Atlantic rift opened along the Ribeira-Araçuai-West Congo Neoproterozoic part of the Pan African orogen (640 Ma) which outcrops in the southernmost part of the study area (e.g., Bento dos Santos et al., 2015; Fossen et al., 2020; Pedrosa-Soares et al., 2008; Salazar-Mora et al., 2018; Stanton et al., 2019; Szatmari & Milani, 2016, and references therein) (Figure 1). At the onset of rifting, the lithosphere was likely thermally equilibrated after 450 Myr of cooling and as thick as adjacent cratonic lithosphere (See Figure S1 in Supporting Information S1). The present day lithosphere thins from north to south in the study area (Figures 3e and 3f). In the north, a fast shear-wave velocity anomaly observed in the mantle evidences a 240–200 km thick lithosphere that continuously extends from onshore below the craton to offshore below the distal margin (Begg et al., 2009; Celli et al., 2020b; Huismans & Beaumont, 2011; Szameitat et al., 2023) (Figure 3e). In contrast, further south, the Angolan shield is not underlain by cratonic lithosphere and is only about 160 km thick (Figure 3e) (e.g., Steinberger & Becker, 2018). The oceanic crust at breakup time has a normal thickness in the central South Atlantic (away from the Walvis ridge) suggesting a normal mantle temperature (Graça et al., 2019; Sauter et al., 2023).

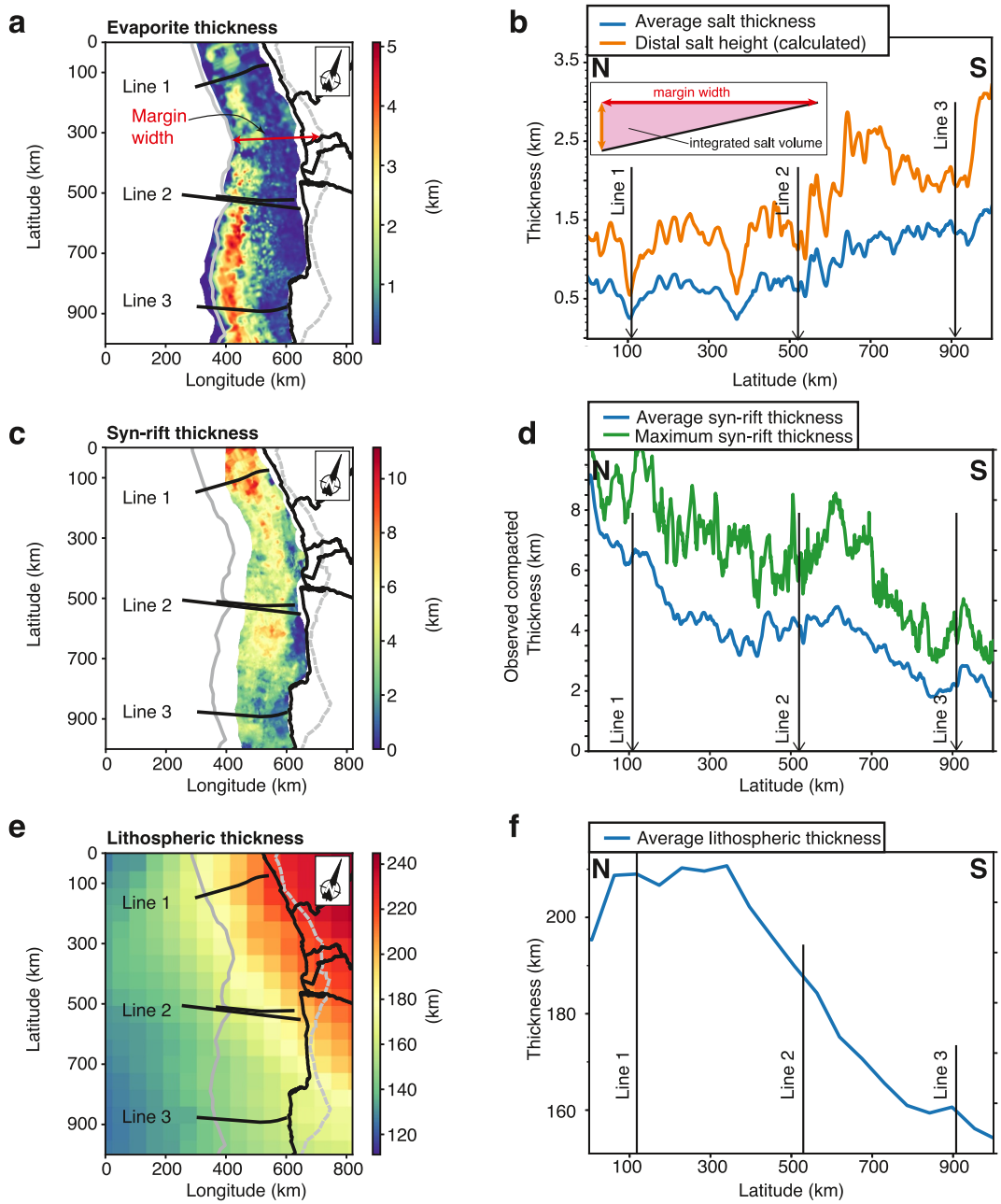

Figure 3. Sedimentary, crustal and lithospheric structure of the African rifted margin. Maps of the vertical thickness of (a) evaporites (Pichel et al., 2023), (c) syn-rift deposits thickness offshore (Pichel et al., 2023), and (e) average lithospheric thickness after Steinberger and Becker (2018). Along strike variations along the rifted margin of average thicknesses of (b) evaporites, (d) syn-rift sediments, and (f) lithosphere. Transverse Mercator projection with central Meridian at 12°E, origin of latitude at 0°N in the WGS-84 reference ellipsoid. Coordinates are shifted and rotated by 20° clockwise. Gray line: continent-ocean boundary; Dashed gray line: most proximal onshore extent of the margin. For line 2, the northernmost and shorter black bold line is the reflection profile from GXT CongoSPAN line 3100 (Pichel et al., 2023) while the other is the refraction profile "7 + 11" from Contrucci et al. (2004) and Moulin et al. (2005).

3. Constraints on Margin Structure

3.1. Data-Set

We constructed three thickness maps of the syn-rift, evaporites, and post-rift deposits along the central South Atlantic African rifted margins (Figure 3 and Figure S2in Supporting Information S1). We selected five

characteristic crustal cross-sections including two conjugate rifted margins: cross-sections 1–1′, 2, and 3–3′ (Figure 4). We used recently published data and interpretations from Pichel et al. (2023) and combined them with other published interpretations of crustal cross-sections at similar locations (e.g., Blaich et al., 2011; Ceraldi & Green, 2017; Clerc et al., 2017; Contrucci et al., 2004; Epin et al., 2021; Fernandez et al., 2020; Gordon et al., 2013; Lavier et al., 2019; Loureiro et al., 2018; Péron-Pinvidic et al., 2015; Romito & Mann, 2022; Strozyk et al., 2017; Unternehr et al., 2010; Zalán et al., 2011). The interpretation of the main horizons (i.e., top evaporites, base evaporites, and top basement) benefits from the dense 2-D seismic surveys (ION GXT 2D CongoSPAN I & II) with a typical spacing of about 10–25 km between each seismic line (Pichel et al., 2023). Along the African rifted margin, we used the interpretation of the crustal structure along cross-sections 1–3 refined using gravimetric and magnetic data, and a large set of subsurface data by Pichel et al. (2023) (Figure 4). Along cross-section 2 (South Congo), we also used deep seismic refraction constraints on crustal structure (Figures 1 and 4) from Contrucci et al. (2004) and Moulin et al. (2005).

3.2. Crustal Structure of the Conjugate Rifted Passive Margins

The geological cross-sections show four crustal domains (Figure 4). (a) The proximal domain is bound onland by the position of the most proximal normal fault associated with syn-rift sediments in the hanging-wall and its crustal thickness varies from 35 to 25 km. (b) The necking domain spans the change in crustal thickness from ∼25 km to 7–10 km. (c) The distal margin spans the thin continental crust (10–0 km). (d) The transitional domain extends from the last well-defined thinned continental crust of the distal margin to the first well-defined oceanic crust. The proximal domain is about 50 km wide and symmetric along cross-section 1–1′ while it is much wider and asymmetric along cross-section 3–3′ (i.e., 170 km on the Africa rifted margin and 80 km on the South American conjugate). The width of the necking zone is similar on all cross-sections (about 30 km). The width of the distal margin for the Camamu, Jequitinhonha, and Espirito Santo basins on the South American conjugate ranges from ∼85–100 km, while it is 100–150 km wide in the Gabon, Congo, and Kwanza margins (Loureiro et al., 2018). The transitional domain width ranges between 35 and 50 km. The total width of the conjugate distal margins, that is, summing distal width of the two conjugates for lines 1–1′ and 3–3′, is consequently about 200 km (Table 1), and about 270 km when including the transitional domain.

The continental crust of the distal margin in South Gabon is between 3 and 11 km thick (6.3 ± 1.9 km on average) (cross-section 1, Figure 4 and Table 1). In the Kwanza basin (cross-section 3), the distal margin crust is 0.5–11 km thick (5.0 ± 3.0 km on average). Seismic refraction data in South Congo (cross-section 2) suggest that the distal margin crust is 5.7–10.4 km thick (7.7 ± 1.3 km on average). The Moho identified from seismic reflection is on average 1–3 km shallower than the one identified from seismic refraction data. This shallower reflectivity might therefore represent an internal continental crustal discontinuity. The oceanic crust is about 5–6 km thick on average while it is ∼8 km in the distal Espirito Santo basin (cross-section 3′ in Figure 4). These thicknesses fall within the range of normal oceanic crust worldwide (Christeson et al., 2019; White et al., 2001).

3.3. Syn-Rift Deposits Thickness and Sediment Routing Systems

The thickness of syn-rift deposits varies along strike of the African rifted margin (Figures 3c and 3d). They are very thick in the South Gabon basin (about 6 km on average) and thinner toward the South (4 km in South Congo to 2 km in Kwanza basins) (Figures 3c and 3d and Table 1). Average evaporite thickness is 600 m in the South Gabon basin while it is about 800 m in the South Congo basin and 1,300 m in the Kwanza basin (Figures 3a and 3b). We estimated along strike variations of the total integrated evaporite volume assuming 20% evaporite dissolution as similarly estimated in the Red Sea (Mitchell et al., 2021). We redistributed the total volume along the margin to reconstruct the evaporite thickness in the very distal margin at the end of deposition. To do this, we assumed a triangular shaped distribution between the proximal and the distal margin (Figure 3d and Figure S3a in Supporting Information S1). The reconstructed evaporite thickness in the distal margin just after deposition varies from 1,200 m in Gabon, 1,600 m in South Congo to 2,400 m in Kwanza. We also extrapolated to the conjugate South American margin by doubling the volume calculated from the West Africa data set (Figure 3a and Figure S3 in Supporting Information S1). The estimated evaporite volume per unit of length along strike increases from $0.45 \cdot 10^9$ m^2 in the North (South Gabon basin) to $1.05 \cdot 10^9$ m^2 in the South (Kwanza basin) (See Figure S3b in Supporting Information S1).

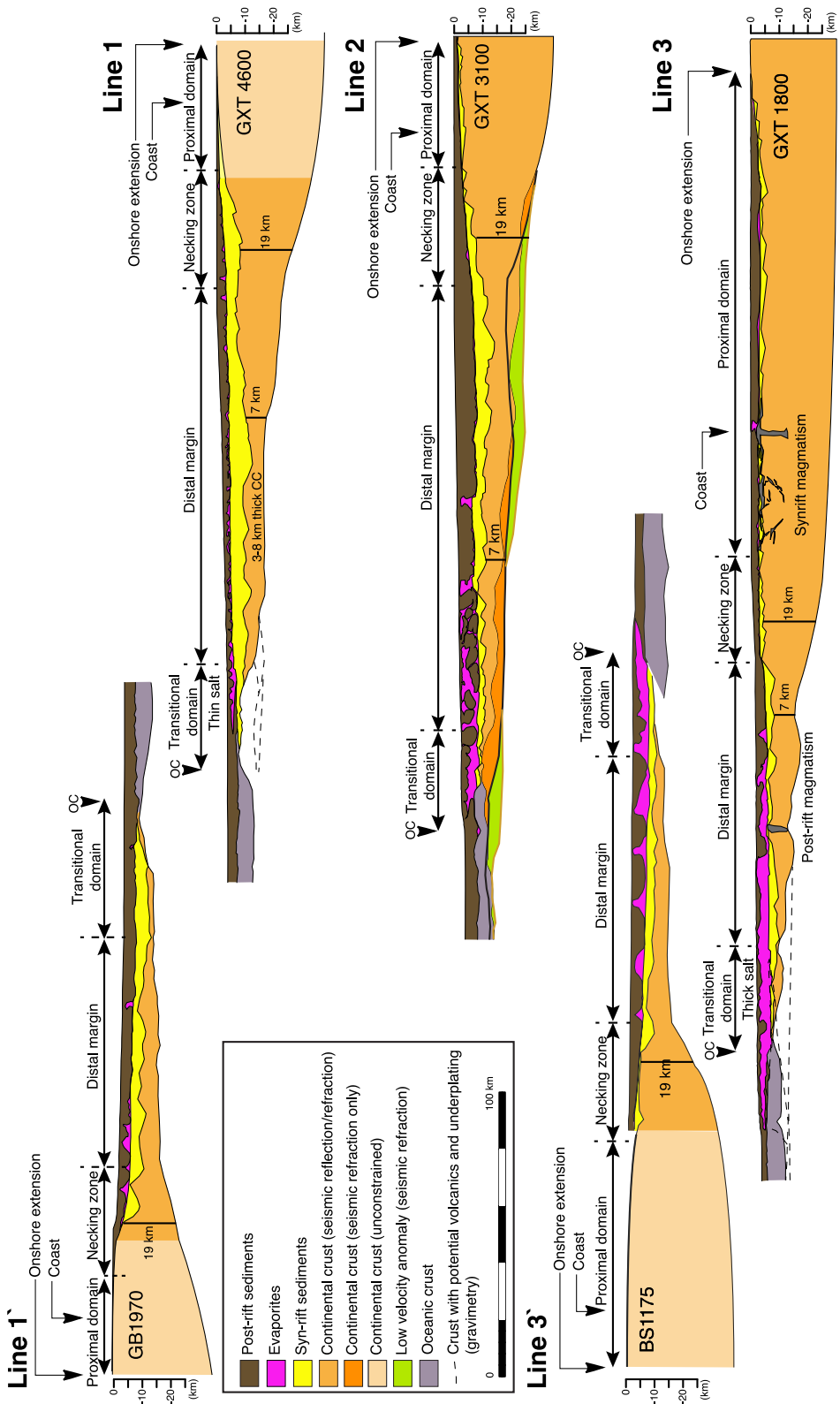

Figure 4. Interpreted crustal cross-sections of the rifted margin of the central South Atlantic. The main horizons (i.e., top evaporites, base evaporites and top basement) result from published interpretation of seismic data (e.g., Pichel et al., 2023). Refraction data on cross-section 2 is from Contrucci et al. (2004). Distal structures from gravimetry (dashed lines) are from Fernandez et al. (2020). See location of crustal cross-sections on Figures 1–3.

Table 1
Syn-Rift Sediment and Crustal Average Thicknesses Along the Distal Margin of the Three Reference Crustal Cross-Sections Along the West Africa Margin

	H_{sed_obs} (km)	H_{sed_unc} (km)	H_c (km)	W (km)	Evap. Vol. ($1e^9 \cdot m^2$)
Line 1 (Gabon)	5.6 ± 1.1	6.1 ± 1.1	6.3 ± 1.9	215	0.6
Line 2 (South Congo)	2.4 ± 1.0	2.9 ± 1.1	7.7 ± 1.3	–	0.9
Line 3 (Kwanza)	1.9 ± 0.9	2.2 ± 1.0	5.0 ± 3.0	195	1.3

Note. Sediment thickness, H_{sed_obs}, corresponds to the syn-rift compacted sediment thickness as observed in the present day seismic profiles between the top basement and the base of evaporites. Uncompacted sediment thickness, H_{sed_unc}, corresponds to the syn-rift sediment thickness unloaded from evaporites, post-rift sediments, and water layers above it assuming clastic sediments and the same compaction law used elsewhere in this study. The compaction law is described in the method section (See also details in Supporting Information S1). H_c is the crustal thickness. The standard deviation is provided for H_{sed_obs}, H_{sed_unc}, and H_c. W is the total distal margin width, that is, summing the width of the two conjugate distal margins (not available for line 2) (Figure 4). "Evap. Vol." is the extrapolated evaporite volume per unit length along strike of the conjugate margins (more details in the text and see Figure S3 in Supporting Information S1).

While the thickness of the syn-rift deposits decreases from North to South, it is relatively constant in the distal margin for a given cross-section (Figures 3 and 4). A lateral source of sediments has been identified in Congo from narrow drainage basins located between the coast line and the rift flanks (Kebi-Tsoumou, 2018). However, the N-S distribution suggests that more clastic sediments were produced and transported to the basin in the North than in the South. A larger onshore catchment area in the North might explain this distribution although not described in the literature. In terms of runoff, most of the studied area was under dry and warm tropical climate, at least during the Aptian, except to the North (Sergipe-Alagoas/North Gabon/Congo) where more humid conditions prevailed promoting fluvial erosion and clastic sedimentation (e.g., Chaboureau et al., 2012; Lentini et al., 2010; Thompson et al., 2015).

4. 2-D Thermo-Mechanical Model Description

The 2-D thermo-mechanical models are set up to allow comparing their results to our central South Atlantic data set to assess conditions of evaporite deposition (margin elevation and water depth). In addition to two reference models without deposition (M1 and M2) we provide six 2-D numerical models (M3-8) that reproduce the observed key characteristics comprising the width of the distal margin, the average syn-rift sediment thickness, the total extension, the average crustal thickness, and inferred magmatic budget at the latitude of the three reference crustal cross-sections 1–1′, 2, and 3–3′ (Figure 4). Two models with a base level of 0 m and −500 m below present-day global sea level are used as end-member scenarios for which the topography of the basin at crustal break-up, that is, the time of evaporite deposition, is used as analog for each cross-section. The forward numerical models of rifted margin formation used here benefits from previous studies where parameters and processes responsible for strain localisation, melt prediction, and isostasy have been calibrated to Earth's conditions (Lu & Huismans, 2022; Theunissen & Huismans, 2019, 2022; Theunissen et al., 2022). The model accounts for decompression melting with feedbacks on temperature, viscosity, and density of the mantle. We calibrated the crustal and mantle densities to match mid-ocean ridge elevation (Theunissen et al., 2022). We design a simple layered setup compatible with inferred mechanical and thermal conditions at the onset of rifting in the central South Atlantic. We summarize in this section the methodology and how the model setup has been designed.

4.1. Method

We use the 2-D finite-element geodynamic code FANTOM to model continental rifting to seafloor spreading (Theunissen & Huismans, 2019; Theunissen et al., 2022; Thieulot, 2011) (See details in Text S1 in Supporting Information S1). The code solves the Stokes and heat equations coupled through P-T dependent rheology and density using an arbitrary Eulerian-Lagrangian formulation (Fullsack, 1995). The model top defines a free surface that is advected at each time step with the velocity field and that can be modified to account for surface processes. We use a Mohr-Coulomb description for plasticity in the brittle layers while non-linear pressure and temperature dependent power law creep is used with parameters for olivine from Karato and Wu (1993) for the mantle and wet quartz from Gleason and Tullis (1995) for the continental crust. Crustal and mantle viscous strength is adjusted by

applying a scaling factor respectively f_c and f_m (See Text S1 in Supporting Information S1). Strain localisation results from plastic strain weakening where initial friction and cohesion are linearly reduced with accumulating strain (Theunissen & Huismans, 2022) (See details in Text S1, Table S1, and Figure S4 in Supporting Information S1).

4.2. Melt Prediction Using Linearized Mantle Solidus

The procedure for prediction of mantle decompression melting is based on a linear mantle solidus approach (Boutilier & Keen, 1999; Lu & Huismans, 2021; McKenzie & Bickle, 1988; Nielsen & Hopper, 2004; Scott, 1992; K. Simon et al., 2009) (See details in Text S1 in Supporting Information S1). The melt model considers depletion and the change of the solidus with increasing total melt fraction. Melt prediction includes the effect of latent heat by melting on temperature, of melt weakening and dehydration strengthening on viscosity, and of melt depletion on density. The model is calibrated to provide a standard 6 km thick oceanic crust during mid-ocean ridge spreading (Christeson et al., 2019; Louden et al., 1996; White et al., 2001). We compute the equivalent melt thickness that is tracked at the surface of the model. We apply a phase change to the upper 6 km of the exhumed sub-lithospheric mantle and set its density to 2,900 kg/m^3, typical for oceanic crust (Carlson & Raskin, 1984; Tenzer & Chen, 2019). We do not directly use the thickness predicted from the melt prediction routine for the phase change because the basic vertical melt extraction routine results in a reduced predicted oceanic crust thickness above the mid-oceanic ridge (e.g., Lu & Huismans, 2021). This simplification avoids the complexities related to melt focusing and ensures that the correct oceanic crust thickness and elevation can be obtained at the mid-ocean ridge, as done in previous studies (Beaumont & Ings, 2012; Theunissen et al., 2022).

4.3. Mechanical Boundary Conditions

The boundary conditions are similar to previous studies (Theunissen & Huismans, 2019; Theunissen et al., 2022). Continental rifting and mid-ocean spreading are modeled by applying extensional velocity boundary conditions in the lithosphere on both model sides. The upper surface is free and the side and bottom boundaries have free-slip boundary conditions. Outflow is balanced by a small distributed inflow on the side boundaries in the sub-lithospheric mantle. In order to ensure constant total mass, the average pressure along the bottom of the model is maintained constant by adjusting the influx of the sub-lithospheric mantle at the sides.

4.4. Isostasy and Base Level

The 2-D geodynamic model ensures gravitational equilibrium of mass in the model's outer layers, satisfying the isostasy assumption similarly to Earth (Theunissen et al., 2022; Wolf et al., 2022). Calibration of the density structure allows reproduction of the observed elevation difference between continents and the mid-ocean ridge on present-day Earth therefore constraining the isostatic response (Theunissen et al., 2022). The difference in overpressure between the continental domain and the mid oceanic ridge at a compensation depth of 250 km in the mantle is small, in the order of few MPa, corresponding to ±10–100 m, indicating that the elevation difference between continents and the mid-ocean ridge is controlled by local isostasy (Theunissen et al., 2022). Because of the boundary conditions, any change in elevation in the model results from deformation and isostasy, with the mid-ocean ridge elevation remaining stable.

Given the stability of model elevation, we define an absolute reference level fixed at 0 m (300 m below the initial model top), corresponding to present-day global sea level, assuming +300 m elevated continents. We assume that undeformed continental lithosphere has an elevation of +300 m with respect to the 0 m reference (present-day global sea level) that serves as a global datum reference. We define the base level as an absolute elevation relative to the 0 m reference that is independent from surface displacement. The base level constrains the accommodation of clastic sedimentation below it. If a water load is included, we assume that the water column reaches base level. If there is no water, the accommodation is defined by base level. Given the assumed isolation of the Central South Atlantic basin from the global ocean, we assume that the base level is local and independent of the global sea level.

4.5. Sedimentation

The base level is used to define the extent of the sedimentary basin as explained in the previous sub-section. We consider the accommodation to be the space available for deposition between the basin floor and the base level

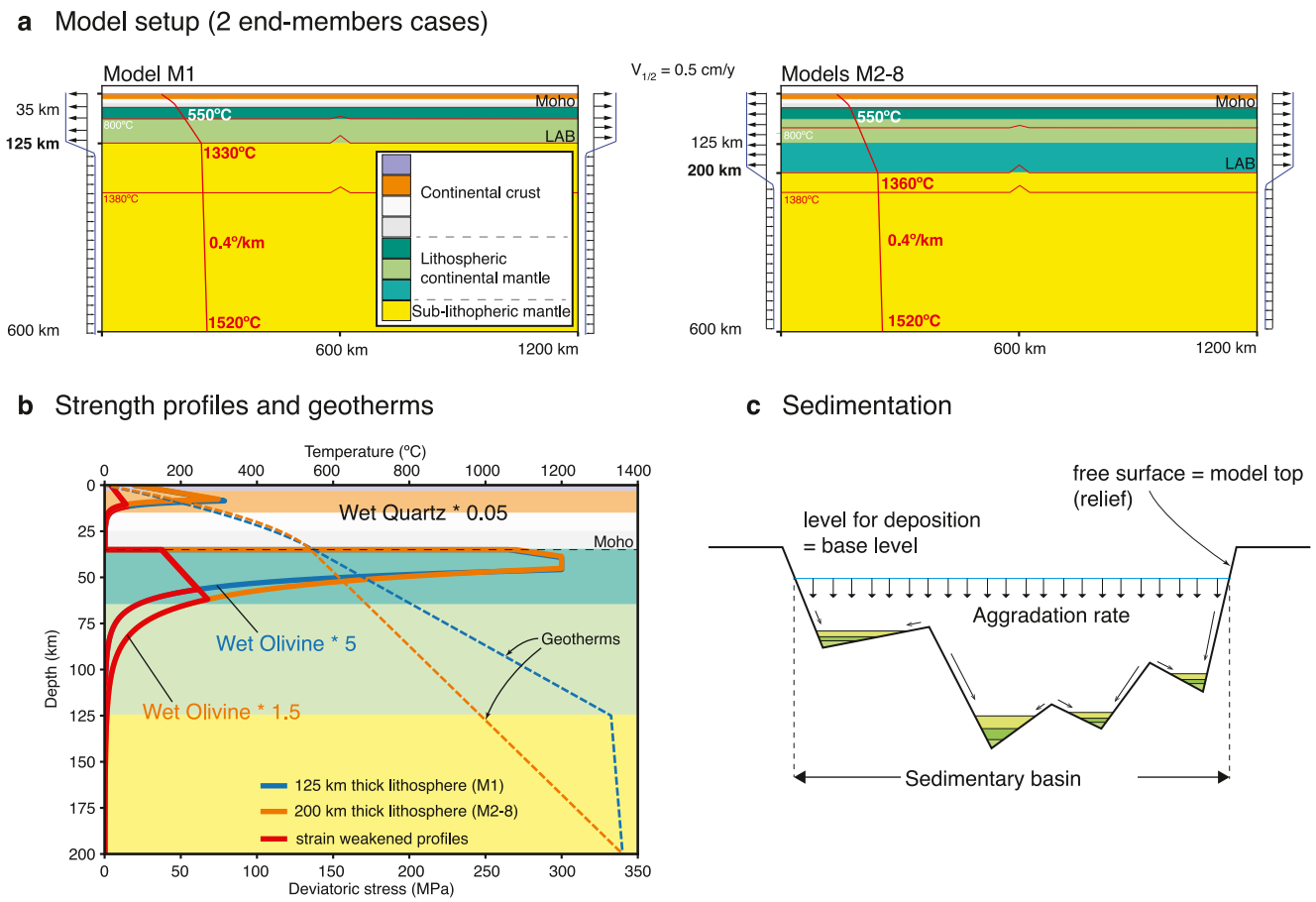

Figure 5. Numerical model setup. (a) Lithospheric scale model setups including thermal and rheological horizontal layering: 125 km (left) or 200 km (right) thick lithosphere. (b) Strength and thermal profiles of the two model setups at model start. Continental crust layers have the same rheology and only serve as markers to track the deformation. Models with thick lithosphere (M2–M8) have a higher crustal heat production to reproduce thermal and rheological crustal profiles of reference 125 km thick lithosphere model M1. The mantle flow law is scaled to also reproduce the mantle strength profile of the reference model M1 (See text). (c) Schematic diagram illustrating syn-rift aggradation algorithm.

and changes of accommodation during continental rifting result from both subsidence and variations of base level elevation through time. Sedimentation is simulated by filling at each time step the accommodation between the free surface, that is, model top, and a prescribed base level with sediments. We consider instantaneous mechanical compaction by vertical loading of sediments (e.g., Theunissen & Huismans, 2019) (See details in Text S1 and Figure S5 in Supporting Information S1). The bulk compaction law employed reproduces average density profiles for clastic sediments (e.g., sandstones and clays) (e.g., Albertz & Ings, 2012; Athy, 1930). We implement kinematic aggradation for syn-rift sediments that fills up local minima in each sub-basin (e.g., Theunissen & Huismans, 2019) (Figure 5c). The rate of sedimentation is constant through time which allows to control the final sediment thickness in the system with one parameter (i.e., average aggradation rate) more easily than with mass conserving onshore erosion that would require to vary two parameters (erodibility and base level). It also allows taking into account that a part of the sedimentation could be potentially controlled by longitudinal feeding which cannot be modeled in a 2-D plane. We do not include erosion and sediment transport in these models.

4.6. Model Setup

The initial model geometry represents a 1,200 km wide and 600 km deep, idealized, crustal and upper mantle rheologically layered lithosphere and sub-lithospheric mantle similarly to previous studies (Theunissen & Huismans, 2019, 2022; Theunissen et al., 2022) (Figure 5). The model domain is discretized using 2,400 × 337 finite elements, leading to spatial resolution of 500 m horizontally and 200 m vertically in the top 18 km, 600 m between 18 and 45 km depth, 1 km between 45 and 125 km depth, 2 km between 125 and 265 km depth and circa

6.5 km in the sub-lithospheric mantle (bottom 335 km). We employ two different lithospheric thicknesses. Model M1 has a 125 km thick continental lithosphere with 35 km thick crust and 90 km thick lithospheric mantle. Models M2–M8 have a 200 km thick continental lithosphere with 35 km thick crust and 165 km thick lithospheric mantle. Model M1 provides a reference for rifting of a Phanerozoic continental lithosphere. Models M2–M8 are designed for comparison with the central South Atlantic. The 200 km thick continental lithosphere represents an average thickness of the inherited depleted continental lithosphere at the onset of rifting assuming a depleted mantle in the narrow corridor formed by the cratonic roots on both sides of the Pan African orogen after 400 My of post-orogenic erosion, thermal equilibration, and secular cooling (See Figure S1 in Supporting Information S1). We use a higher continental crustal heat production in models with thicker lithosphere compared to model M1 to have the same initial crustal temperature structure and same initial crustal strength profile. As margin width depends to first order on crustal strength (e.g., Lavier et al., 2019; Theunissen & Huismans, 2019), this allows models M2–M8 (200 km thick lithosphere) to be comparable with model M1 especially in terms of margin width. We also reduce viscous strength of the continental lithospheric mantle for models with colder thick lithosphere to have a similar initial strength profile compared to model M1 (Figure 5b).

The thermal structure includes an adiabatic gradient of 0.4°C/km in the sub-lithospheric mantle and a potential mantle temperature of 1,280°C that is in the range of current estimates on Earth. The side boundaries are insulated and the bottom boundary has a fixed temperature boundary condition of 1,520°C. This results in a temperature of 1,330°C at the base of the 125 km thick lithosphere (model M1) and 1,360°C at the base of the 200 km thick lithosphere (models M2–M8). We prescribe radiogenic production in the continental crust resulting in a Moho temperature of 550°C and in a surface heat flow of ∼60 mW/m^2. This heat flow is comparable with present-day predicted heat flow in the outer part of the Congo Craton and in the Proterozoic orogenic belts where lithospheric thickness is lower than 250 km (Al-Aghbary et al., 2022). Given that breakup occurred along the Pan African suture and given an initial lithospheric thickness of 200 km, a heat flow of ∼60 mW/m^2 is reasonable. We use constant thermal conductivity of 2.25 W/m/K in all materials, heat capacity equals 1,270 J/K/kg in the mantle and 1,050 J/K/kg in the continental and oceanic crust. These values allow fitting the surface heat-flow. The initial temperature is laterally uniform except at the lithosphere-asthenosphere boundary where a small thermal anomaly is included to promote lithospheric necking in the center.

We use a reference density for the fertile sub-lithospheric mantle of 3,280 kg/m^3 and average depletion buoyancy in the continental lithospheric mantle of −26.5 kg/m^3 for the 200 km thick lithosphere and −15 kg/m^3 for the 125 km thick lithosphere. It is well established that the continental lithospheric mantle is depleted in heavy elements (Al, Ca, Fe, Si) and more buoyant than the sub-lithospheric mantle (asthenosphere) that is more fertile (e.g., Griffin et al., 1999, 2008; Lamb et al., 2020; Schutt & Lesher, 2006; Theunissen et al., 2022, and references therein). The thermal and density structures provide a calibrated reference mid-ocean ridge elevation that corresponds to about −2,000 m air-loaded elevation and equivalently to a −2,900 m deep water-loaded mid-ocean ridge with a continental elevation of +300 m (e.g., Theunissen et al., 2022) (Figure 6 and Figure S6 in Supporting Information S1).

We apply the same full extension rate of 1.0 cm/year to all models by using the same half velocity of 0.5 cm/year extension rate in the lithosphere on both model sides. In models M1–M8 shown in the main text we do not include water load because observations suggest limited water depth during the syn-rift. Base level for sedimentation and sedimentation rate vary between the models. Models M1 and M2 do not have deposition, models M3–M5 have deposition with a base level fixed at the 0 m reference representing present-day global sea level (i.e., 300 m below initial model top) and models M6–M8 have a base level fixed at −500 m below present-day global sea level (i.e., 800 m below initial model top).

4.7. Evaporite Deposition

Late syn-rift evaporite deposition is modeled by restarting models M6 (analog for Gabon) and M8 (analog for Kwanza) just before crustal breakup. In these models, water load is included during evaporite deposition, assuming a gradual connection of the basin to the global ocean. We consider two end-member scenarios of evaporite deposition with either significant transient base level drop before deposition and progressive base level increase during evaporite deposition (scenario 1) or a fixed high base level (scenario 2). In both cases, evaporite deposition stops after 2 Myr when the total volume reaches the reconstructed total volume of evaporites at a given latitude as observed in the data. Based on present-day natural examples, it is commonly assumed that evaporite

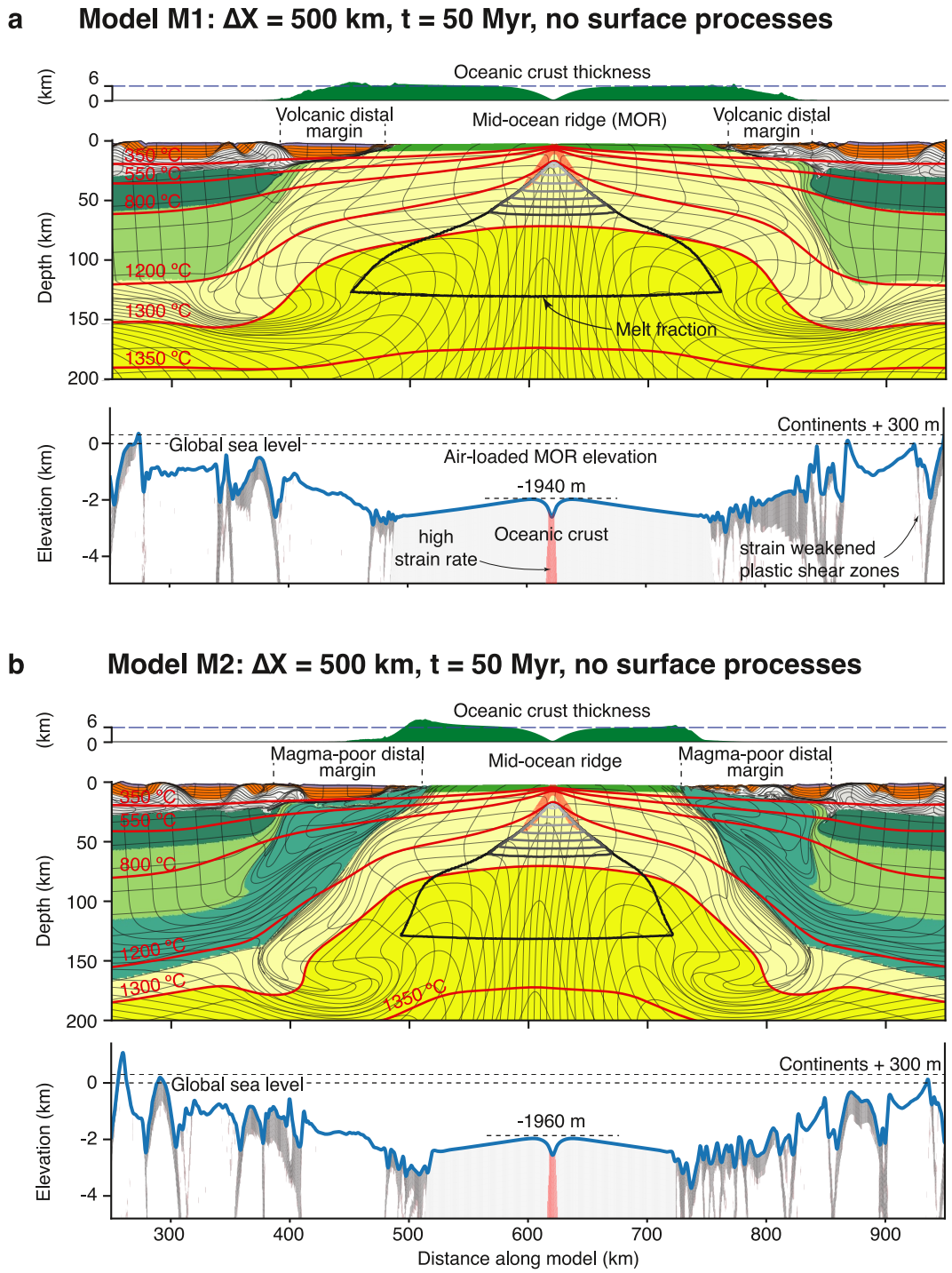

Figure 6. Numerical models M1 (a) and M2 (b) after 50 Myr of extension (1 cm/year full extension rate) without surface processes and water load. For each model: (1) top section: melt prediction shown as equivalent oceanic crust thickness (green), (2) mid section: model color code is provided in Figure 5a, isotherms are in red, gray contours beneath the mid-ocean ridge axis are total melt fraction extracted after decompression melt production in the melt window (every 2%), (3) bottom section: free surface elevation (=model top) with vertical exaggeration of about 20 (thick blue line). Light gray is the ocean crust. Gray patches are strain weakened plastic shear zones and red patches are high strain rate zones.

Table 2
Key Characteristics of the Six Reference Numerical Models Described in This Study

	Agg. rate (cm/year)	Base level bsl (m)	Margin width (km)			H_{sed} (km)	H_c (km)
			Prox.	Neck.	Distal	Ave.	Ave.
M3	0.025	0	105	35	255	1.9	9.8
M4	0.05	0	120	15	260	3.3	9.8
M5	0.15	0	130	15	260	5.9	8.7
M6	0.5	−500	105	20	265	6.3	7.2
M7	0.1	−500	110	30	260	3.4	7.6
M8	0.05	−500	95	35	230	1.7	8.2

Note. M5 and M6, M4 and M7, and M3 and M8 are respectively analog for crustal cross-sections 1–1′ (Gabon), 2 (South Congo), and 3–3′ (Kwanza) respectively (Figure 10). Proximal, necking and distal domain widths, and distal margin sediment thickness (H_{sed}) and crustal thickness (H_c) are computed at crustal breakup time (30 Myr). The average sediment thickness H_{sed} provided here can be directly compared with the uncompacted sediment thickness from the observations (Table 1 and Figure S12 in Supporting Information S1). Agg., aggradation; bsl, below present-day global sea level; ave., average.

deposition necessarily occurs in brines in which the water depth is less than 100 m (e.g., Warren, 2016, and references therein). In scenario 1, we therefore assume evaporite aggradation between the seafloor and a continuously and linearly rising base level and that there is evaporite deposition only when the bathymetry (water depth) is lower than 100 m. The initial base level is −1,600 m below present-day global sea level and the rate of base level rise is 0.65 mm/year. In scenario 2, the aggradation rate and the base level are fixed to respectively 1 mm/year and −400 m below present-day global sea level. At each time step, the evaporites are wrapped on the seafloor and the new topography slightly diffused (500 m^2/year) without erosion of the previous one to favor aggradation in local minima. Although aggradation rate is fixed, there is no evaporite deposition when the accommodation, defined between the seafloor and the fixed base level, is completely filled. The evaporites are treated as a linear viscous material with a constant viscosity of 10^{18} Pa.s. The low viscosity of 10^{18} Pa.s. is an end-member case to assess the maximum syn-evaporite deposition flow owing to their own weight.

5. Thermo-Mechanical Modeling Results

We first describe in this section models M1–M2 without sedimentation and the sensitivity of these models to key parameters that control margin width, crustal thickness and magmatic budget, that is, spreading rate, crustal and mantle flow laws, and potential mantle temperature. We then describe models M3–M8 with sedimentation. Reference parameters for all models are summarized in Table 2.

5.1. Reference Model M1 Without Sedimentation

Reference model M1 has a lithospheric thickness of 125 km. We show model M1 at 50 Myr after 500 km of extension (Figure 6a. See Movie S1 for full model evolution). At this stage, the oceanic domain is 270 km wide and the predicted steady-state oceanic crust thickness is 6 km. Stretching on both margins is distributed over a 200 km wide domain on each conjugate: a ∼120 km wide proximal domain with crustal thinning accommodated by large offset normal faults exhuming mid-crust and a 80 km wide distal domain with abrupt crustal thinning, beneath which the continental mantle lithosphere is removed. The distal margin is composed of upper-crustal rafts separated by exhumed mid- and lower-crust. Predicted melt thickness increases progressively along the distal margin to a thickness of ∼6 km. In the oceanic domain, spreading and mantle melting are stable and symmetric. The proximal margin is on average −1,000 m deep with fault related footwall highs and hanging wall basins. The distal margin progressively deepens to ∼−2,500 m (i.e., 2.5 km below sea level) with a sharp transition to the oceanic domain that has a smooth topography (Figure 6a). The air-loaded mid-ocean ridge is at ∼−1,950 m elevation (given 300 m elevated continents). When water load is applied to this model, the mid-ocean ridge elevation is ∼−2,900 m (given a base level at the 0 m reference elevation) in agreement with the calibration procedure and the isostasy concept (See supplementary model SM1 and Figure S6a in Supporting Information S1). We note here that rifted margin formation in this model exhibits three phases (Movie S1): (a) distributed extension over a wide area during ∼9 Myr, (b) progressive necking in the distal margin concomitant with mantle

lithosphere removal and decompression melting of the sub-lithospheric mantle, and (c) crustal break-up and establishment of a mid-ocean ridge spreading system.

5.2. Model M2 With Thick Lithosphere Without Sedimentation

Model M2 is characterized by a 200 km thick continental lithosphere. We show model M2 at 50 Myr after 500 km of extension (Figure 6b and Movie S2). The main difference between models M2 and M1 is the propensity for counter-flow of weak depleted lower mantle lithosphere into the necking area created by upper mantle lithospheric thinning. Counter-flow of depleted mantle lithosphere below the distal margin suppresses and delays mantle melting. Extension on both margins is, similarly to M1, distributed over 200 km on each conjugate. The distal margins in M2 are 100–130 km wide, that is, 20–50 km wider compared to M1, with a narrower oceanic domain and delayed lithosphere break-up. The distal margins show no melt, in contrast to model M1, and progressively increasing melt thickness in a domain of depleted lower mantle lithosphere that is exhumed to the surface, preceding the oceanic domain. The topography has similar characteristics as in model M1.

Supplementary models SM3-SM16 show sensitivity to varying spreading rates, crustal and mantle rheology in order to evaluate their control on margin width and melt production (See Figure S7 in Supporting Information S1). Distal margin width increases with decreasing crustal strength and with spreading rate (Figure S7a in Supporting Information S1). The rheology of the depleted lower continental lithospheric mantle controls the efficiency of mantle counter-flow during rifting. A weak lower continental lithospheric mantle favors efficient counter-flow beneath the margin and possible oceanward exhumation of the lithospheric mantle (Figure S7c in Supporting Information S1). Counter-flow is relatively insensitive to spreading rate (Figure S7b in Supporting Information S1).

We also test sensitivity of model M2 to potential mantle temperature T_p to evaluate its effect on the elevation difference between continents and mid-ocean-ridge (MOR) and on the regional continental elevation during rifting (See Figure S8 in Supporting Information S1). A higher mantle temperature decreases the depth of the oceanic domain, increases oceanic crustal thickness and depletion buoyancy of the oceanic mantle lithosphere associated with larger melt extraction. However, it does not affect the relative elevation between the distal continental margin and the continent compared to the reference model M2.

5.3. Models 3–5 With Sedimentation

We now use the setup of model M2 and include deposition with varying sediment aggradation rate from 0.025, 0.050, to 0.150 mm/year in models M3, M4, and M5 respectively, all with a base level of 0 m (e.g., representing present-day global sea level). We show the models after 300 km of extension ($t = 30$ Myr), that is, close to or at crustal breakup time. We first describe model M3 and provide key structural and thermal characteristics with their time evolution during continental rifting (Figure 7), and then show how increasing sedimentation rate affects basin architecture in models M4 and M5 (Figure 8).

At crustal breakup model M3 exhibits a 600 km wide basin that can be divided into three domains: proximal margin, necking zone, and distal margin (Figure 7a). The proximal margin domain starts from the first normal fault where the crust is thinned by upper-crustal extension and middle to lower crustal flow, extends to the necking zone, and is about 120 km wide on each conjugate. The necking zone, that corresponds to the sharp transition of Moho depth between proximal and distal domains, is 30–80 km wide. The distal margin is 120 km wide on each side (Figures 7 and 8a). Sedimentation widens the distal margin compared to the reference model M2 without sedimentation by about 50–60 km for sedimentation rates higher than 0.05 mm/year (See Figures S7d and S7e in Supporting Information S1). We extract the evolution of four key characteristics for each of the domains: (a) average crustal thickness, (b) average surface heat flux, (c) average sediment thickness, and (d) average elevation (Figure 7 and Movie S4). Model M3 exhibits three syn-rift stages. Stage 1 (0–9.4 Myr) corresponds to the initial distributed extension where crustal thickness slowly decreases from 35 to 27 km in each of the domains, with moderately varying heat flux. Average elevation and sediment thickness show accommodation creation filled by sediment accumulation after an initial phase of crustal thinning and efficient subsidence in the center of the model (i.e., future distal margin) around 4 Myr (Figure 8a). Topography in the basin is close to zero and sediment thickness in the distal margin is limited by accommodation. Stage 1 ends with the rupture of the upper continental mantle and the initial emplacement of weak depleted lower lithosphere at the base of the crust in the necking area. Stage 2 (9.4–16 Myr) is characterized by a rapid decrease of crustal thickness, a rapid increase of surface heat flux

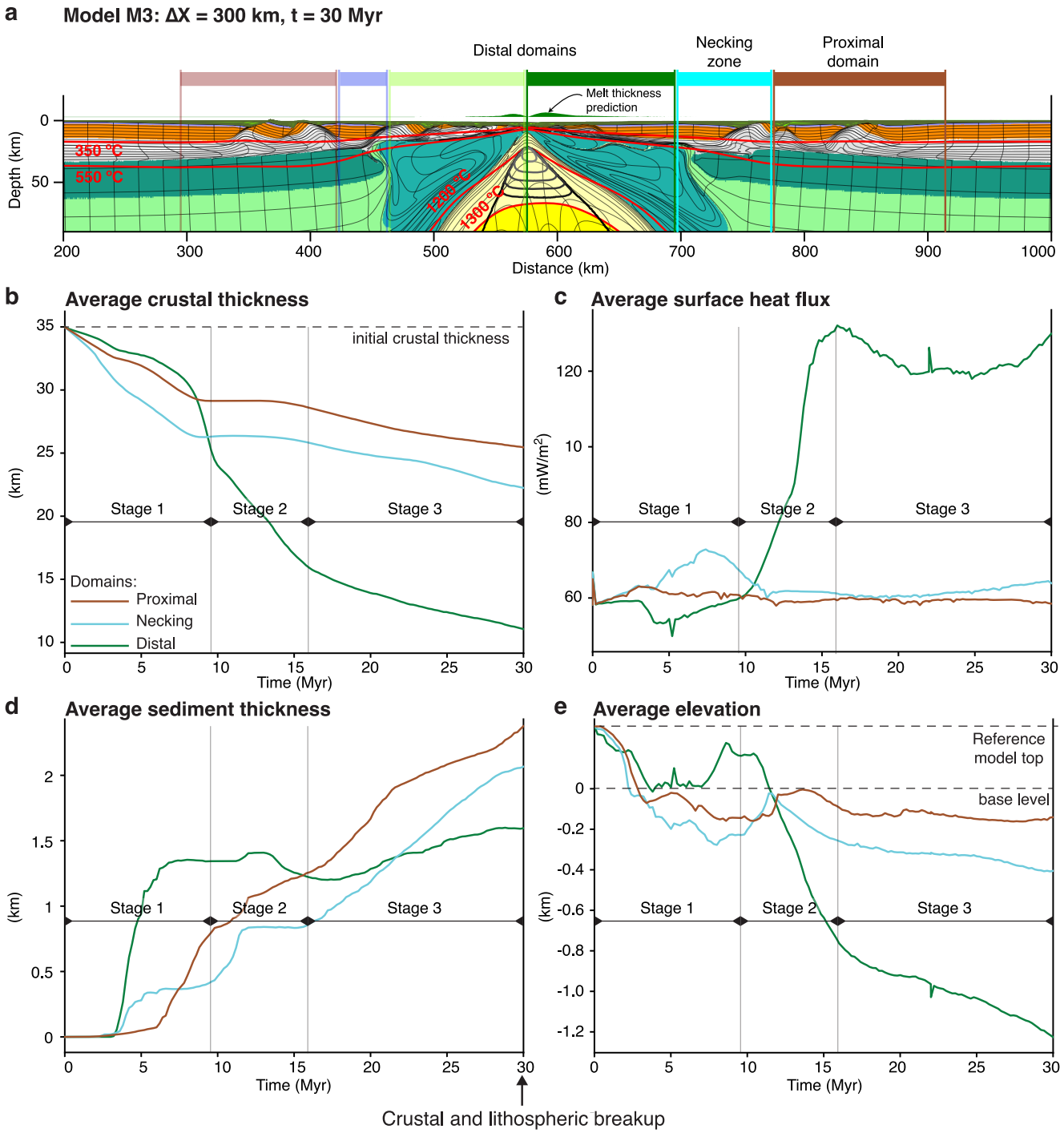

Figure 7. Numerical model M3 at crustal breakup time after 30 Myr of extension (1 cm/year full extension rate) with sedimentation and without water load showing the limits of the three genetic domains (a). Isotherms are in red, color code is provided in Figure 5. Syn-rift evolution of (b) the average crustal thickness of each genetic domain of the right margin, (c) of the average surface heat flux, (d) of the average sediment thickness deposited, and (e) of the average elevation. Reference model top is the top of the computation grid, that is, free surface, and corresponds to the elevation of the continents, that is, +300 m. Base level at 0 m corresponds to the present-day global sea level. The curve filled with green color on top of each model represents the melt prediction displayed as equivalent oceanic crust thickness and the blue dashed line above it is the reference 6 km thick oceanic crust.

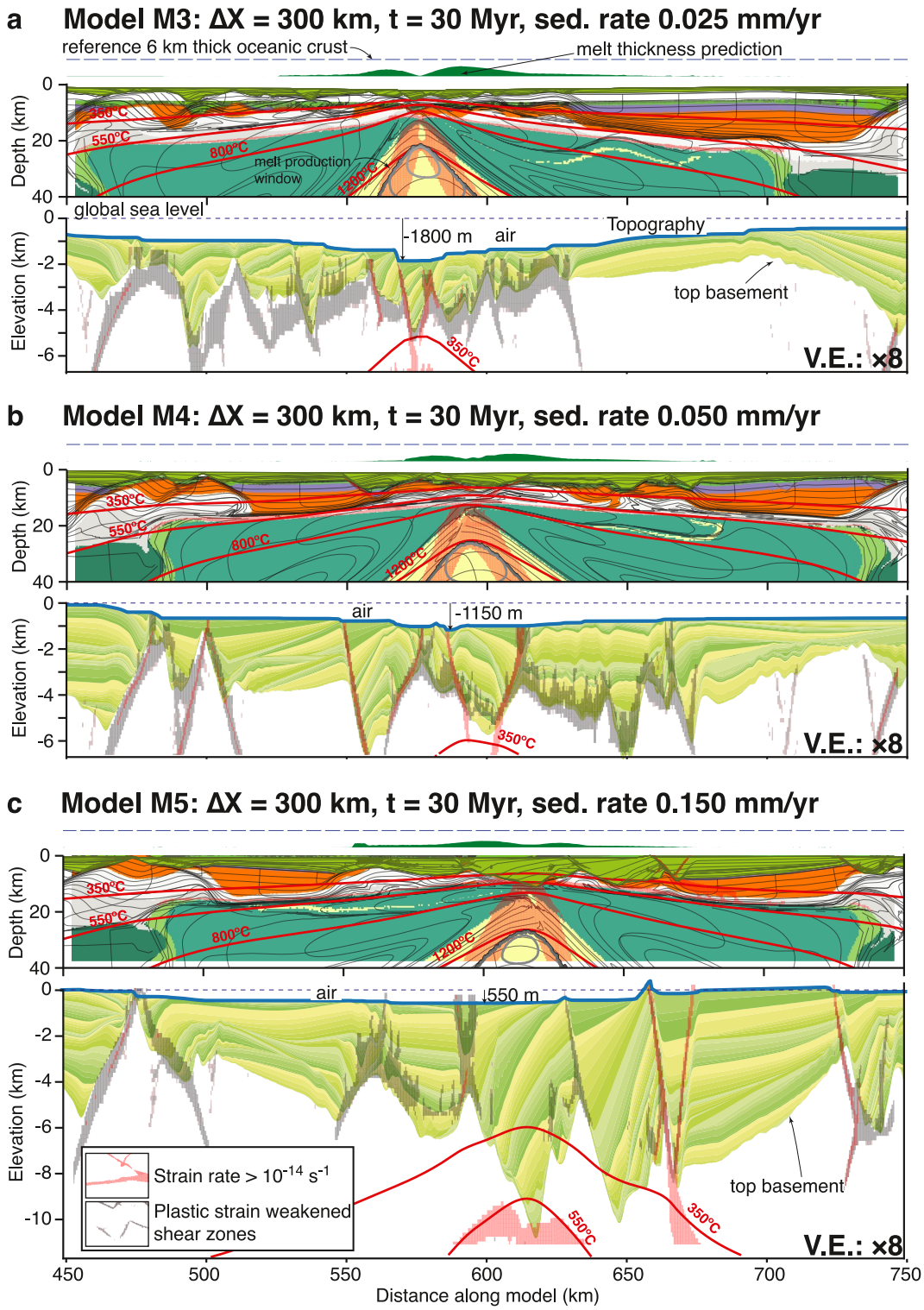

Figure 8. Zoom on the distal domain of numerical models (a) M3, (b) M4, and (c) M5 at crustal breakup time after 30 Myr of extension (1 cm/year full extension rate) with sedimentation and without water load. Isotherms are in red, color code is provided in Figure 5. Aggradation rates increase from top to bottom. On top, melt prediction is displayed as equivalent oceanic crust thickness (green curve). At the bottom, the free surface (model top, thick blue line) and the sedimentary architecture are shown with a vertical exaggeration of 8. The alternation pattern of green colors in the sediments is repeating every 400 Kyr.

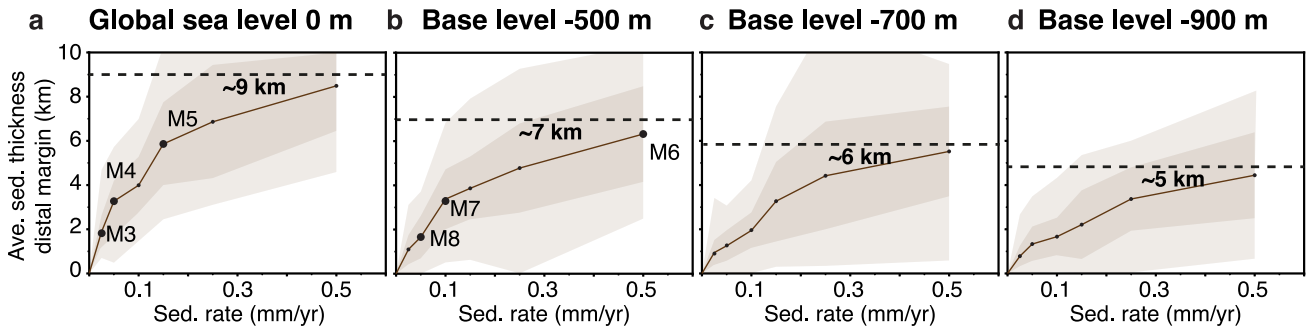

Figure 9. Sensitivity of the average sediment thickness in the distal margin to base level and sedimentation rate in a 200 km wide domain centered on the thermal necking zone at 30 Myr shown in Figure 8. (a) Reference case with base level at the 0 m reference (present-day global sea level). Other panels show same plot with base levels at: (b) −500 m, (c) −700 m and (d) −900 m below present-day global sea level. Dark and light gray shades give the standard deviation and the extremum values respectively. Black dot represents the result of each independent model. Dashed line represents the maximum possible average sediment thickness in the distal margin.

associated with increase of Moho temperature, and rapid deepening of the distal margin. The proximal margin and necking domains undergo little crustal thinning during stage 2. Average sediment thickness increases slowly in the proximal margin and necking domain, progressively filling accommodation. Sediments in the distal margin are actively extended after deposition with average sediment thickness remaining constant or decreasing during this time interval. At the end of stage 2, the distal margin is completely underlain by depleted lower continental mantle lithosphere. Stage 3 (16–30 Myr) is characterized by distributed extension over the whole rift, with progressive thinning of the distal margin leading to breakup at 30 Myr. Average elevation of the distal margin at breakup is −1.2 km while the proximal and necking domains are shallower (−100 m and −300 m respectively). We note that syn-rift magmatism is suppressed by counter-flow of the depleted mantle lithosphere below the distal margin. At breakup, the sub-lithospheric mantle produces initial melt accreted to the most distal continental crust.

In model M3, the distal margin shows deformed, variable thickness (1.9 ± 0.9 km), sediments with a complex faulted basement and a deep air-loaded basin (−1,800 m at the most distal edge of continental crust) (Figure 8a and Table 2). Models M4 and M5, with a higher sedimentation rate, exhibit very similar characteristics as M3 but progressively thicker sediments, 3.3 ± 0.9 km and 5.9 ± 1.9 km respectively, and decreasing basin depth with air-loaded elevations of −1,150 m and −550 m at the most distal edge of the continental crust in models M4 and M5 respectively (Figures 8b and 8c and Table 2). We note that the topographic difference between the proximal and distal domains of the margin of model M5 (~500 m) is very low compared to models M3 and M4.

5.4. Sensitivity of Model Results to Base Level

We next explore how the average sediment thickness in the distal margin depends on the aggradation rate and the base level. We vary aggradation rate systematically between 0 and 0.5 mm/year, with a base level of 0, −500, −700, and −900 m below present-day global sea level (Figure 9). For each base level, the average sediment thickness in the distal margin tends to a maximum related to the available accommodation. For the 0 m base level (i.e., present-day global sea level), maximum average sediment thickness tends to about 9 km (dashed line in Figure 9a) while for a base level of −900 m available accommodation limits average sediment thickness to ~5 km. Models with a base level lower than −600 m below present-day global sea level cannot reproduce sediment thickness in South Gabon distal margin (Section 1–1′) (Figure 9 and Figure S9 in Supporting Information S1).

Given these results with low, intermediate, and high aggradation rate, we consider models with a base level of 0 and −500 m as end-member scenarios for which we can compare the topography of the basin at crustal breakup, that is, the time of evaporite deposition (Figure 10). We first describe and compare models M5 and M6 (high sedimentation rate models). Model M5 topography, with a base level of 0 m, shows that the proximal margin and necking zone fill with sediments up to base level whereas accommodation in the distal margin is not completely filled by sediments and exhibits a flat topography of about −500 m (Figures 8c and 10a). Model M6, with a base level of −500 m, exhibits a flat topography from the proximal to the distal margin and an accommodation that is almost completely filled with sediments (Figure 10a and Figure S10a in Supporting Information S1). We note

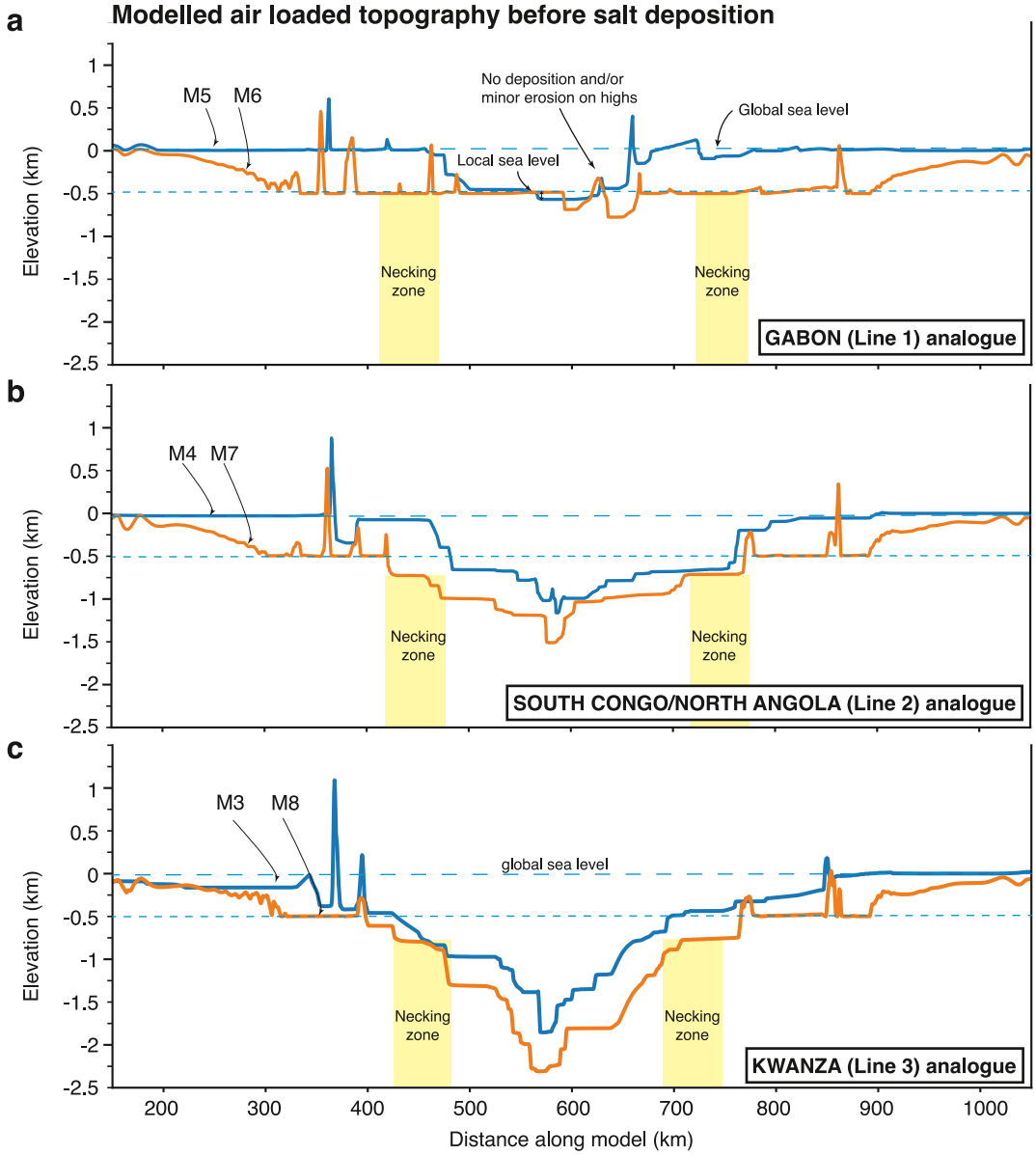

Figure 10. Air loaded topography at crustal breakup in our models (t = 30 Myr). Base level is fixed at the 0 m reference (present-day global sea level) for models M3, M4, and M5 (thick blue line) and at −500 m below present-day global sea level for models M6, M7, and M8 (thick orange line). Distal margin width, average crustal thickness, and average sediment thickness in the distal margin are compatible with observations along the three crustal cross-sections of the African rifted margin (Tables 1 and 2, and Figure S12 in Supporting Information S1). Models M5 and M6 are therefore considered as analog for Gabon (a), models M4 and M7 for Congo (b), and models M3 and M8 for Kwanza (c).

normal fault footwall highs from the proximal to distal margin in both models. We next describe models M4 and M7 with intermediate sedimentation rate. Model M4 topography (base level 0 m) exhibits a proximal domain filled with sediments up to base level with a rapid transition across the necking zone to a deep distal margin with an air-loaded average elevation of −800 m (Figures 8b and 10b). Model M7 (base level −500 m) exhibits flat topography at base level elevation (i.e., −500 m below present-day global sea level) in the proximal domain where the basin is filled by sediment with a rapid transition to the deep distal margin that shows an air-loaded average elevation about −1,100 m (Figure 10b and Figure S10b in Supporting Information S1). Finally, models M3 (base level 0 m) and M8 (base level −500 m) with low sedimentation rate show under-filled margins and a progressive deepening from the proximal to the distal margin to maximum air-loaded elevation of −1,800 and −2,250 m respectively (Figures 8a and 10c and Figure S10c in Supporting Information S1).

5.5. M6 and M8 With Evaporite Deposition

We next simulate late syn-rift evaporite deposition by restarting models M6 and M8 at 28 Myr (i.e., about 2 Myr before crustal breakup), respectively analog for South Gabon and Kwanza, because they represent the two end-members with high and low syn-rift sediment thickness and because they provide accommodation for evaporite deposition in the proximal domain in contrast to the equivalent models M5 and M3 (Figure 10). We explore two different scenarios for evaporite deposition in order to evaluate relations between basin geometry, evaporite distribution, and total evaporite volume. In scenario 1, we assume an initial base level at −1,600 m elevation below present-day global sea level that allows for water load in the most distal margin and no evaporite deposition for bathymetry over 100 m, followed by a linear base level rise to about −300 m after 2 Myr. Evaporite deposition occurs for water depths shallower than 100 m, filling available accommodation to base level. In scenario 2, base level is fixed at −400 m below present-day global sea level and evaporites are aggraded in local minima with a rate of 1 mm/year at any water depth.

In model M6, scenario 1 results in progressive filling up of the basin with evaporites on-lapping the proximal margin (Figure 11a). Evaporite deposition is stopped after 800 Kyr, when the total volume reaches $0.5 \cdot 10^9$ m^2 (per meter along strike length), consistent with observations from Gabon (Figure 3 and Figure S3 in Supporting Information S1). At this stage the top of the evaporites is −270 m below present-day global sea level. We note feedback between evaporite deposition and fault activity with high offset normal faulting in the most distal margin and evaporite thickness of 5–6 km. Model M8 (scenario 1) starts with a base level at −1,600 m below present-day global sea level resulting in a pre-existing 100 km wide lake in the distal margin that has a bathymetry of maximum 1,000 m and on average 500 m. As evaporite deposition is limited to areas shallower than 100 m, the distal margin shows no evaporites throughout its evolution, forming two separate evaporite basins on each conjugate margin. When the evaporite volume in model M8 is consistent with the volume observed in the Kwanza margin, the evaporites extend onto the proximal domain and the base level at the end of evaporite deposition is at −270 m elevation after 2 Myr (Figure 11b). In this scenario, oldest evaporites are limited to the distal margin.

For both models M6 and M8, scenario 2 results in progressive filling of the entire basin synchronously from the proximal to the distal margin in 2 Myr (Figure 12). The evaporite basin is continuous between the two conjugate margins but exhibits a central lake. In model M6, the central lake is small (e.g., 40 km wide) and shallow (bathymetry of about 150 m on average) while, in model M8, the central lake is about 200 km wide and up to 2,000 m deep (Figure 12a). In scenario 2, the oldest evaporites can be found from the proximal to the distal margin. We note that feedback between evaporite deposition and fault activity results in high offset normal faulting in the most distal margin and evaporite thickness of 5–6 km in both models M6 and M8. Model M8 with thin syn-rift sediments has more accommodation available from the proximal to mid-distal margin for evaporite deposition compared to model M6 with thick syn-rift sediments (Figure 12b). The thickness of the evaporite is therefore larger in model M8 (e.g., 1.5–3.5 km) than in model M6 (e.g., 750 m to 1.5 km). We note that, for model M8, scenario 2 results in much more evaporite deposition in the distal margin than scenario 1.

6. Discussion

6.1. General Model Behavior

Similarly to previous studies, our models show that crustal strength provides a primary control on the total margin width (e.g., Brune et al., 2017; Buck, 1991; Huismans & Beaumont, 2011, 2014; Lavier et al., 2019; Theunissen & Huismans, 2019; Theunissen et al., 2022) (See Figure S7 in Supporting Information S1). A strong crust promotes narrow necking and early breakup of both crust and mantle lithosphere, while a weak crust decouples upper-crustal deformation from localized mantle lithosphere necking leading to wide rifted margins. In this case, extension in the crust is distributed over a wide area with large offset normal faults in the thin brittle upper-crust and efficient flow of the weak viscous middle and lower crust, that is, models M2-8 (Figures 6 and 8, and Figure S10 in Supporting Information S1). The width of the distal margin varies from 100 to 150 km at 1 cm/year full extension rate, and increases with decreasing crustal strength and increasing extension velocity (See Figure S7a in Supporting Information S1). Deposition enhances fault offset and lower crustal flow leading to formation of multiple upper-crustal rafts that result in a wider margin with increasing sedimentation rate (Theunissen & Huismans, 2019) (See Figures S7d and S7e in Supporting Information S1).

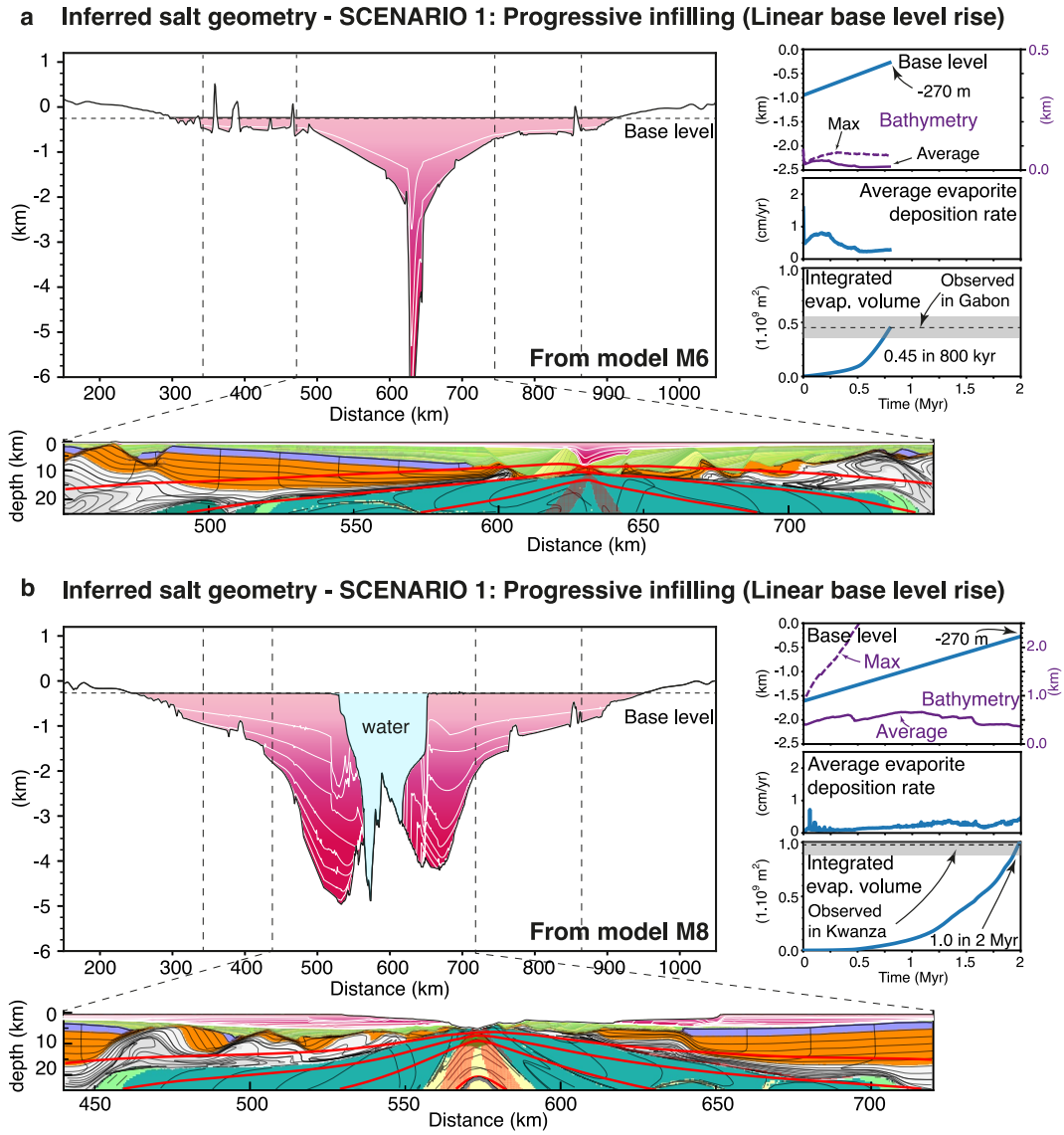

Figure 11. Numerical models with evaporite deposition based on scenario 1: deep initial base level and linear base level rise. (a) Scenario 1 with model M6 (thick syn-rift sediments, analog for the Gabon rifted margin): evaporite aggradation from the deepest part of the basin (∼−900 m) and progressive filling up of the basin until evaporite volume is consistent with observations in the South Gabon basin. (b) Scenario 1 with model M8 (thin syn-rift sediments, analog for the Kwanza rifted margin): the initial base level is −1,600 m below present-day global sea level and evaporite deposition is allowed only for water depth <100 m. For each model, evolution through time of base level elevation below present-day global sea level, average bathymetry (purple curve, scale on the right axis), average evaporite deposition rate, and accumulated evaporite volume is shown. During evaporite deposition extension rate is 1 cm/year as in all models in this study. Evaporite viscosity is 10^{-18} s^{-1}. White lines in the evaporites represents the stratigraphy every 200 Kyr.

The wide rifted margin of reference model M1 exhibits highly depth dependent thinning, where the continental lithospheric mantle breaks before the crust, leading to decompression melting and melt accretion to the distal margin (Figure 6a) (e.g., Huismans & Beaumont, 2011, 2014; Lu & Huismans, 2022). In contrast, models M2 to M8 that include thick depleted lithospheric mantle exhibit counter-flow of the lower part of the lithosphere into the necking zone suppressing mantle melting. The degree of lower lithospheric counter-flow depends on its viscosity and density (See Figures S7b and S7c in Supporting Information S1) (e.g., Beaumont & Ings, 2012; Huismans & Beaumont, 2011, 2014; Lu & Huismans, 2022). Models with highly efficient counter-flow exhume depleted lower mantle lithosphere beyond the distal edge of the continental crust, and delay the onset of magmatic oceanic spreading. In contrast, inefficient counter-flow produces only partial underplating of the distal margin

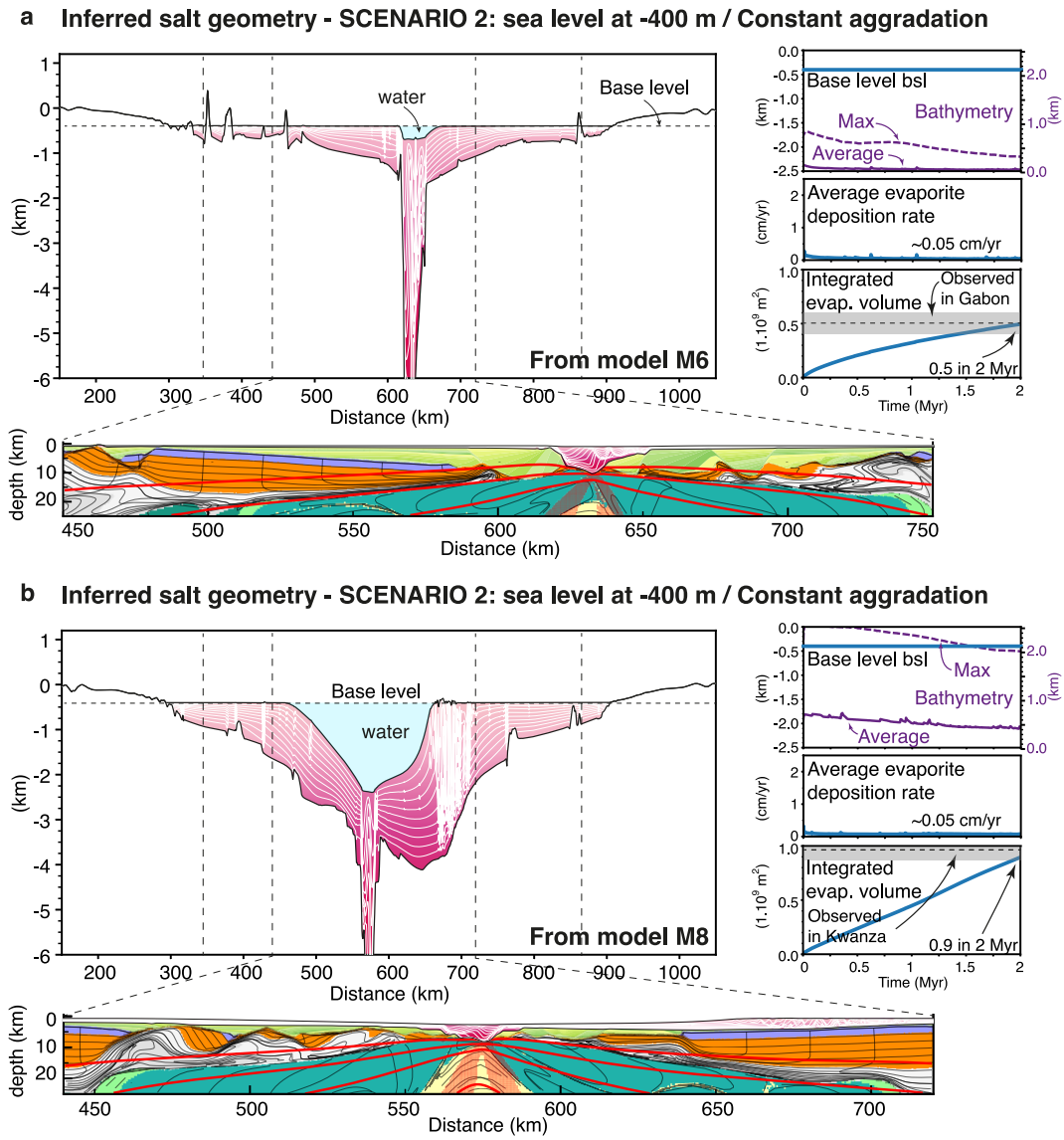

Figure 12. Numerical models with evaporite deposition based on scenario 2: fixed base level of −400 m below present-day global sea level, constant aggradation rate of 1 mm/year. (a) Scenario 2 with model M6 (thick syn-rift sediments, analog for the Gabon rifted margin): evaporite aggradation and progressive filling up of the basin until evaporite volume is consistent with observations in the South Gabon basin. (b) Scenario 2 with model M8 (thin syn-rift sediments, analog for the Kwanza rifted margin). For each model, evolution through time of base level, average bathymetry (purple curve, scale on the right axis), average evaporite deposition rate, and accumulated evaporite volume is shown. During evaporite deposition extension rate is 1 cm/year as in all models in this study. Evaporite viscosity is 10^{-18} s^{-1}. White lines in the evaporites represents the stratigraphy every 200 Kyr. Although aggradation rate is fixed, there is no evaporite deposition when the accommodation, defined between the seafloor and the fixed base level, is completely filled.

with depleted mantle and leads to a transition from a magma-poor to a magma-rich distal margin (See Figure S7c in Supporting Information S1).

The primary innovation of this study lies in utilizing a 2-D thermo-mechanical model with calibrated mantle densities and a constrained isostatic response to predict the absolute elevation of the distal margin during continental rifting (Theunissen et al., 2022). The model results can therefore be used to predict the elevation of the distal margin and the available accommodation and to explore the respective contributions of water load, syn-rift sediment thickness, and potential mantle temperature on them. The topography in model M2 without deposition varies from ∼−1 km in the moderately extended proximal margin and necking zone, progressively deepening in

the distal margin to −2.2 km at the transition with the oceanic crust. In these models, the oceanic spreading center has an air-loaded elevation of ∼−1,950 m. Models that include deposition show a smoother topography with an elevation controlled by both the rate of deposition and the base level. With a high deposition rate, the basin is filled up to base level resulting in a flat topography from the proximal to the distal domain. In contrast, with a low deposition rate, accommodation is filled in the proximal margin, but not in the distal margin that has an air-loaded elevation of −1.5 to −2 km. Sensitivity tests demonstrate that the distal margin is systematically significantly deeper than the proximal margin, even with an anomalously hot upper-mantle, except if the sediment deposition rate is high. These results are similar to previous published 2-D geodynamic modeling results and to elevations predicted from simple lithospheric thinning models coupled with isostasy (McKenzie, 1978; Svartman Dias et al., 2015). However, previously published 2-D geodynamic models only qualitatively described relative subsidence or stratigraphic response to sedimentation and have never been used to quantitatively compare sediment volume and distribution with observations (Burov & Poliakov, 2001; Pérez-Gussinyé et al., 2020; Svartman Dias et al., 2015) (See next sections).

We use our models to evaluate late syn-rift evaporite deposition scenarios (Figures 11 and 12). In scenario 1, that assumes an initial base level drop and evaporite deposition for shallow water (<100 m), we calibrated the rate of base level rise and the initial base level to provide a scenario of 2 Myr long diachronous evaporite deposition consistent with the volume observed in the Kwanza and South Gabon basins. While the evaporites fill the space between the base level and the seafloor, the subsidence, related to lithospheric cooling, crustal thinning, isostatic response and sediment compaction owing to evaporite loading, result in variations of evaporite aggradation rate and bathymetry during deposition. Evaporites are initially deposited in the distal margin and progressively on-lap the proximal margin. This results in a diachronous deposition of evaporites from the distal to the proximal margin. Evaporite deposits are thinner where syn-rift sediments are thicker and are deposited faster (e.g., model M6, analog for Gabon, 800 Kyr) compared to where syn-rift sediments are thinner (e.g., model M8, analog for Kwanza, 2 Myr) (Figure 11). We note that starting with a base level from the deepest part of the basin in model M8, about −2,250 m below present-day global sea level, results in extreme 10 km thick evaporites in the distal margin and none in the proximal domain and necking zone which does not reproduce evaporite deposition on-lapping the proximal margin (Figure S11 in Supporting Information S1). In scenario 2, that assumes a fixed high base level (−400 m below present-day global sea level) and evaporite deposition at any water depth, we calibrated the base level and the aggradation rate in models M6 and M8 to provide a scenario of 2 Myr long synchronous evaporite deposition that is also consistent with the volume observed in the Kwanza and South Gabon basins. Evaporites are uniformly deposited from distal to proximal in the entire evaporite basin with the same aggradation rate but limited by the available accommodation. This implies a deposition of evaporites coeval in the distal and in the proximal margin.

6.2. Comparison Between Numerical Models and Observations

We next compare the (a) distal margin structure, (b) distribution of magmatism during continental rifting, (c) sediment distribution and base level, and (d) evaporite distribution from models M3-5 and M6-8 (Figures 8 and 10–12, Tables 1 and 2, and Figures S10 and S12 in Supporting Information S1) with the three reference South Atlantic crustal cross-sections (Figure 4).

Models M3-8 are characterized by a 240 km wide conjugate distal margins compatible with the observations (Figures 4 and 8, Tables 1 and 2). The average crustal thickness of the distal margin in the models is 1–2 km thicker than observed along the three reference crustal cross-sections (Tables 1 and 2, and Figure S12 in Supporting Information S1). Given uncertainties on the geometry of the continental crust in the distal margin, we assume that the crustal thickness distribution in the distal margin of the models is a reasonable first order approximation. The topographic evolution of these models can thus be used to infer first order changes in elevation and accommodation in the central South Atlantic during continental rifting and to evaluate late syn-rift evaporite deposition scenarios.

The counter-flow of continental lithospheric mantle observed in our models is compatible with the high seismic shear velocity offshore of the Congo craton in the Northern part of the central South Atlantic, interpreted as "continental material" under the rifted margin (Begg et al., 2009; Celli et al., 2020b; Huismans & Beaumont, 2011; Szameitat et al., 2023), and provides an explanation for (a) the magma-poor character of the central South Atlantic margin in the study area, and (b) the presence of small domains of exhumed mantle in the distal

margin of the South Gabon rifted margin suggested by Epin et al. (2021). Late Aptian kimberlites in Angola suggests the presence of a thick cratonic root adjacent to the Kwanza margin during breakup times similarly to Gabon and Congo (Figure 1) (Celli et al., 2020a).

Average sediment thicknesses of models M3/M8, M4/M7, and M6/M8 are consistent with decompacted syn-rift sediment thickness (i.e., unloaded from evaporites and post-rift sediments) of the three selected cross-sections 1–1′ (Gabon), 2 (South Congo) and 3–3′ (South Kwanza) respectively (see Figure S12 in Supporting Information S1). While the constant aggradation assumption used in our models does not allow catching the complexity of sedimentary basin architecture, the simulated sedimentary basins exhibit features similar to observations. In models with sedimentation, the late syn-rift is not deformed until halfway along the distal margin, consistent with the sag basin observed in the study area (Karner et al., 2003). High sedimentation rates enhance strain localisation and large offset normal faults in the very distal margin, as also observed in the study area (Figure 8) (Clerc et al., 2017; Pichel et al., 2023).

In our models, the depression formed during continental rifting in the distal domain is much deeper than the space required for evaporite deposition given their volume observed along the West African margin (Figure 10 and Text S2 and Figure S13 in Supporting Information S1). Observed evaporite thickness in the proximal domain varies from 50 m to about 1 km (Gindre-Chanu et al., 2022; Pichel et al., 2023). In models M3–M5, with a base level fixed at the 0 m reference, the proximal margin is filled up with pre-evaporite sediments and initial accommodation is not sufficient for proximal evaporites to be deposited. In models M6–M8, the −500 m base level during syn-rift leaves sufficient accommodation for evaporite deposition from distal to proximal margin (Figures 10–12). In both end-member scenarios 1 and 2 of evaporite deposition, evaporite thicknesses in the proximal margin are compatible with observations on the African margin, that is, up to 1,000 m thick evaporites (Gindre-Chanu et al., 2022; Pichel et al., 2023). In the distal margin, feedback between evaporite loading and fault activity locally generates high offset normal faulting with a 5 km thick evaporite basin that is comparable with observations in the distal Gabon margin where 4–5 km of evaporites are found on top of the exhumed mantle and on syn-rift sediments next to long offset normal faults (Epin et al., 2021). Thick evaporites with large offset normal faults are also inferred in the distal margin of the Kwanza basin (Pichel et al., 2023). Distribution of evaporites in models M6 and M8 obtained with both scenarios 1 and 2 are, to first order, compatible with observations in Gabon and Kwanza basins respectively. We note that in these models the evaporite mobility is limited during their deposition despite the low viscosity used for the evaporites.

6.3. Implications for the Central South Atlantic

After crustal breakup, variations in oceanic crust thickness in the study area fall within the standard range (4–8 km) (Graça et al., 2019; Sauter et al., 2023) (Figure 4). This suggests the absence of a regional upper-mantle thermal anomaly at the time of crustal breakup. This implies that the elevation of the distal margin was not affected by an upper-mantle thermal anomaly beneath the central South Atlantic (See Figure S8 in Supporting Information S1).

The evaporite deposition scenarios 1 and 2 have highly contrasting implications for the Kwanza and Gabon margins of the central South Atlantic. Scenario 1, with an initial base level of −1,600 m below present-day global sea level and no evaporite deposition for water depths larger than 100 m, implies a 500 to 1,000 m deep lake in distal margin of the Kwanza case (e.g., Model 8, Figure 11b). The deep lake in the Kwanza case results in separate evaporite basins between the conjugates whereas the Gabon case is characterized by a continuous evaporite basin. The progressive infilling with evaporites from the distal to proximal margin implies diachroneity with only youngest evaporites in the proximal margin. Considering that the Kwanza and Gabon basins are connected and share the same base level, when evaporites begin deposition in Kwanza at −1,600 m below present-day global sea level, the Gabon margin, characterized by thick syn-rift sediments, is initially sub-aerial, with its distal margin at −900 m (e.g., Model 6, Figure 11a). In this Scenario 1, varying topography due to syn-rift sediment thickness also implies diachroneity of evaporite deposition, progressing from the deep Kwanza case in the South to the shallow Gabon case in the North. Scenario 1 allows for regional erosional features at the base of the evaporites as the models suggest sub-aerial conditions from proximal to mid-distance on the margin for both the Kwanza and Gabon cases (Figure 11). Scenario 2 represents another end-member with a fixed base level of −400 m below present-day global sea level at the onset of evaporite deposition and allows for evaporite deposition at any depths. This second scenario results in a more uniform evaporite distribution from the proximal to the distal margin in

both cases (Figure 12). This scenario implies a continuous evaporite basin in the Kwanza case between the conjugates, similar to the Gabon case. The uniform aggradation rate in scenario 2 implies synchroneity of evaporite deposition from proximal to distal margin and from the South to the North. However, the limited accommodation in the proximal margin during evaporite deposition suggests that the youngest evaporites are formed in the distal margin in this scenario 2 in contrast to scenario 1. We note that scenario 2 is incompatible with the pre-evaporite unconformity as interpreted by Karner and Gambôa (2007) and Karner et al. (2003) from proximal to mid-distance on the margin. This suggests a significant initial base level drop just before evaporite deposition consistent with scenario 1 (Figure 13b). While we cannot exclude scenario 2, we favor scenario 1.

We summarize the implications of modeling for base level changes in the central South Atlantic (Figure 13). The basins of the central South Atlantic show a regional sedimentation hiatus in the Aptian in the proximal to mid margin indicating non-deposition and erosion, consistent with a base level below global sea level during the Early Aptian (e.g., Behar et al., 2021; Brownfield & Charpentier, 2006; Chaboureau et al., 2013; Quirk et al., 2013). This observation is compatible with a base level of −500 to −600 m below present-day global sea level during late syn-rift distal margin formation inferred from our models. A deeper base level is not possible because the accommodation in the South Gabon case would not be sufficient for the observed thick syn-rift sediments (e.g., Figure 9 and Figure S9 in Supporting Information S1). The transition phase (at the end of the syn-rift), with the deposition of the undeformed sag basin sediments in the proximal and distal margin, as observed along the rifted margins of the central South Atlantic, suggests a transient moderately increasing base level (few tens to hundreds meters). Thermal subsidence in the most proximal margin onshore is not sufficient to explain sag deposits in the moderately incised valleys (e.g., Behar et al., 2021; Delhaye-Prat et al., 2016; Gindre-Chanu et al., 2016; Kebi-Tsoumou, 2018; Moragas et al., 2023; Van Eden, 1978). The numerical models presented here test two end-member scenarios for base level and subsequent evaporite deposition consistent with observations. Scenario 1 suggests a significant base level drop with a progressive increase of base level that allows evaporite aggradation from the distal to proximal margin (Figure 11). In contrast, scenario 2 suggests that the base level was fixed at about −400 m below present-day global sea level resulting in coeval evaporite deposition from the proximal to the distal margin. In both scenarios 1 and 2, late-syn-rift evaporite deposition in the distal margin suggests influx of sea water into a deep basin (i.e., base level at ∼−1,600 m below present-day global sea level and rising during subsequent evaporite deposition for scenario 1 or fixed base level at −400 m below present-day global sea level for scenario 2) controlling sea water volume and composition during evaporation (Hsü, 1972; Konstantinou et al., 2023; Montaron & Tapponier, 2010; Schmalz, 1969; Tucker, 1991). Numerical models M6 and M8 with evaporite deposition also suggest a base level of −300 to −400 m below present-day global sea level just after evaporite deposition (e.g., Figures 11 and 12). The −300 to −400 m base level below present-day global sea level at the end of evaporite deposition implies post-evaporite sea water influx with base level rising connecting the basin to Cretaceous global sea level (Figure 13). This could explain shallow water conditions during post-evaporite carbonate deposition in the proximal to mid-distal margin (e.g., Marton et al., 2000; Rebelo et al., 2021; Séranne & Anka, 2005).

The two scenarios of evaporite deposition imply distinct environmental conditions, including variations in water depth, salt composition, and salt distribution. The differences in composition of evaporites that would be expected between these scenarios may lead to varying internal evaporite viscosity and density. Although not investigated in this study, post-rift sediment deposition would likely result in contrasting post-rift salt tectonic behavior. For instance, different viscosity, density, and thickness of the allochthonous salt may lead to different advancements of allochthonous salt sheets and salt diapirism. Comparing models that would test these contrasting scenarios with present-day observations could offer additional insights to evaluate the most plausible evaporite deposition scenario. Further investigations are needed to explore these implications.

Integration of modeling results with geophysical and geological observations therefore suggests that along strike variations in evaporite thickness and topography at crustal breakup time are largely controlled by pre-evaporite sediment thickness variations and local base level changes.

6.4. A Mechanism for Base Level Drop Before Evaporite Deposition

Assuming that the Central South Atlantic rift system was disconnected from the global ocean during the syn-rift, the volume of water in the basin was controlled by run-off and evaporation, resulting in a local base level at or above approximately −600 m below present-day sea level (bsl) based on modeling results (Figure 13a). However,

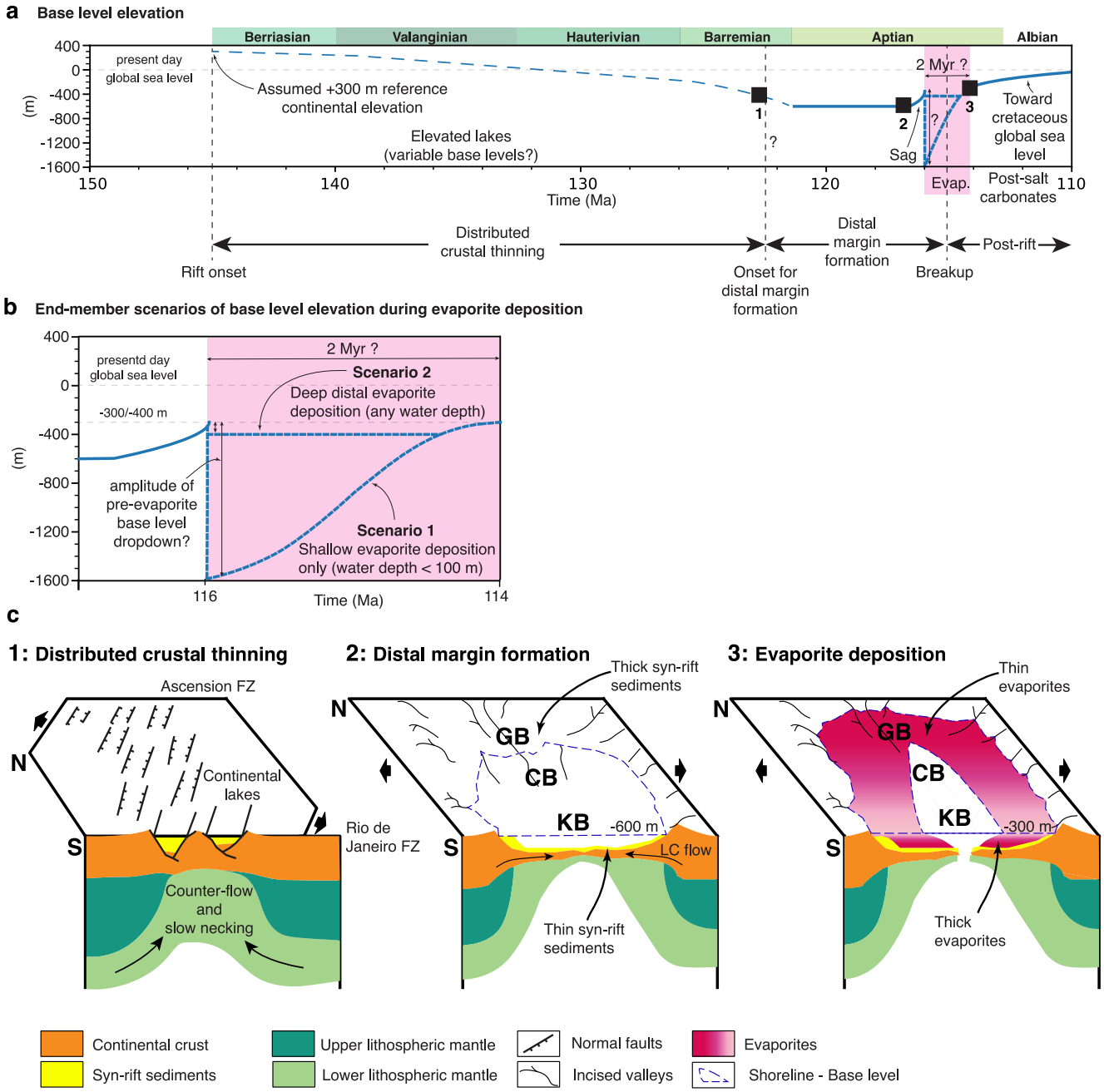

Figure 13. Base level changes through time during formation of rifted margins in the central South Atlantic inferred from modeling. (a) Base level curve (blue line) inferred from the integration of modeling results with geophysical and geological observations. The age of the onset of distal margin formation is obtained by using the total accumulated extension evolution based on kinematic reconstruction of Matthews et al. (2016) (Figure 2b) assuming that the distal margin formation starts after 100–120 km total extension as observed in the numerical models presented in this study. We assume that the time of crustal breakup is 115 Ma and that the period of evaporite deposition is 2 Myr long and centered on the time of crustal breakup. (b) Close up view of the end-member scenarios of base level elevation during evaporite deposition. (c) 3-D block diagrams showing the topography evolution in the Aptian from (1) the phase of distributed deformation to (2) the end of the phase of distal margin formation just before and (3) just after evaporite deposition. The black squares along the base level elevation curve (panel a) gives the approximate time of each 3-D block diagram. GB, Gabon basin; CB, South Congo basin; KB, Kwanza basin; LC flow, lower crustal flow; FZ, oceanic fracture zone; Evap., Evaporites.

determining the amplitude of the pre-evaporite base level drop is challenging (Figure 13b). This study allows for quantifying two end-member scenarios that could explain the volume and distribution of observed evaporites. Evaporites could have been deposited with either a fixed base level at −400 m bsl or with a significant base level drop at −1,600 m bsl, or possibly something in between. The primary processes influencing base level changes

include (a) freshwater input from rivers; (b) evaporation; (c) basin geometry and accommodation, influenced by an increased extension rate during distal margin formation, (d) climatic conditions, and (e) sea water influx during late syn-rift and post-rift. The relative importance of these processes is poorly constrained. A possible mechanism for base level draw-down may be the acceleration of rifting during distal margin formation that may generate more accommodation than freshwater input. Combined with dry conditions and efficient evaporation, this would result in a drop of the local base level in the rift segment.

6.5. Model Limitations

We have used a constant extension rate which represents the average over the duration of rifting in the central South Atlantic (Figure 2). Despite this simplification, the final geometry of the modeled basin matches key observations such as crustal and syn-rift deposits thicknesses, and distal margin width. A constant aggradation rate in the models also provides sufficient accuracy as we focused on reproducing the average syn-rift sediment thickness. However, understanding specific features of South Atlantic basin stratigraphic architecture would require more sophisticated depositional models including sediment transport and carbonate deposition. We have modeled the distribution and general geometry of the evaporite deposits, assuming different end-member scenarios of water depth and deposition rate, and constant viscosity and density for the evaporites. We did not link environmental conditions of evaporite deposition with their composition. However, we acknowledge that this could provide some constraints on the viscosity and density of evaporites, allowing modeling of different post-rift scenarios that are not tested in this study. The modeled basin provides only a first order approximations of the natural system and does not exactly reproduce crustal thinning geometry, basin stratigraphy, and evaporite deposition processes. Nonetheless, the models do provide significant insight into the range of likely basin shapes at the time of evaporite deposition, into possible base level change through time, and how syn-rift sediment accumulation affects evaporite thickness distribution in the distal margin.

7. Conclusion

We use 2-D forward dynamic models to explore the formation of wide magma-poor rifted margins with an application to the central South Atlantic. We explore the conditions for evaporite deposition at the time of crustal breakup in terms of absolute elevation of the distal margin and base level changes. We evaluate competing controls on distal margin width, average sediment thickness and average crustal thickness in the distal margin, total extension, and magmatic budget to reproduce observations at the latitude of the three reference crustal cross-sections. Based on our forward models, we conclude that the observed along strike variations in evaporite basin geometry, evaporite thickness distribution, and inferred distal margin topography and bathymetry are largely controlled by the interaction of base level changes through time and syn-rift sediment supply to the margin. Our main conclusions are:

1. Models of wide rifted margin formation predict early rupture of the upper-mantle lithosphere leading to decompression melting and melt accretion in the distal margin. Models that include thick depleted mantle lithosphere show counter-flow of depleted lower lithosphere inhibiting significant melting beneath the distal margin. They are consistent with, and may provide an explanation for, the magma-poor nature of the Central South Atlantic Gabon, Congo, and Kwanza rifted margins.
2. Syn-rift sediment accumulation controls the seafloor elevation of the distal margin. Six kilometer thick syn-rift sediment results in a shallow air-loaded elevation of about −600 m in the distal margin (i.e., South Gabon basin), while 2 km thick syn-rift sediments results in an air-loaded elevation up to about −2,000 m at crustal breakup time (i.e., Kwanza basin).
3. Modeling results suggest that base level changes during distal margin formation in the Aptian can explain erosional features and depositional environments observed along the rifted margins of the central South Atlantic. A base level about −600 m below present-day global sea level during distal margin formation creates enough space (combined with subsidence) for evaporite deposition in the proximal margin and may explain the Early Aptian erosional features and depositional hiatus observed in the proximal and necking domains. Late syn-rift evaporite deposition can be explained either by a base level drop to −1,600 m below present-day global sea level and evaporite deposition only in shallow water conditions (<100 m) during subsequent progressive rise of base level, or by a base level fixed at −400 m below present-day global sea level with constant aggradation rate and deep water evaporite deposition in the distal margin is allowed. A base level of

about −300 to −400 m at the end of evaporite deposition and a subsequent rise to Cretaceous global sea level explain shallow water conditions and early post-rift carbonate deposition.

4. The two end-member scenarios for base level evolution tested in this work allow matching the volume of evaporites observed along the Central South Atlantic margins. They have, however, highly contrasting implications. A deep base level at the start of evaporite deposition implies (a) progressive aggradation from the distal margin toward the proximal margin, (b) oldest evaporite in the distal margin and youngest in the proximal, (c) a deep lake separating the salt basins between the conjugates for the Kwanza case, and (d) regional erosional features along the base of the evaporites. In contrast, a shallow base level implies (a) coeval deposition and similar ages of evaporites from the proximal to the distal margin, (b) youngest evaporites in the most distal margin, (c) a continuous evaporite basin between the conjugates in both the Kwanza and Gabon case, and (d) limited to absent erosional features along the base of the evaporites. While both scenarios are permissible, the regional erosional features at the top of syn-rift suggest a deep base level at the start of evaporite deposition.

Data Availability Statement

All data are available in the main text or Supporting Information S1. Grids of vertical thicknesses of syn-rift sediments, of evaporites, and of post-rift and forward 2-D numerical model animations are accessible through a figshare repository (Theunissen et al., 2024). Seismic reflection data along or next to the five interpreted crustal cross-sections in this study can be found in the literature following references provided in the text. Numerical models are computed with published methods, described in the Methods section and Supporting Information S1.

Acknowledgments

This study is funded through the COLORS project by TotalEnergies. We thank Uninett Sigma2 for computing time of project NN4704K. We thank Alexandre Pichat, Etienne Legeay, Leonardo Pichel, François Guillocheau, Vincent Delhaye-Pratt, William Vetel, François Sapin, Michael Denis, Marie-Eva Epin, Pierre Masse, Frank Despinois, Tristan Cornu, Frank Peel, Gang Lu, and Sebastian Wolf for stimulating discussions and their help at different stages of this study. We thank Oyvind Natvik and IT department of the University of Bergen for computational resources and help. We thank the editor Dr Michael Bostock, the associate editor Dr Pietro Sternai, and the two anonymous reviewers for their insightful and constructive feedback, which significantly contributed to the improvement of this manuscript.

References

Al-Aghbary, M., Sobh, M., & Gerhards, C. (2022). A geothermal heat flow model of Africa based on random forest regression. *Frontiers in Earth Science*, *10*, 981899. https://doi.org/10.3389/feart.2022.981899

Albertz, M., & Ings, S. J. (2012). Some consequences of mechanical stratification in basin-scale numerical models of passive-margin salt tectonics. *Geological Society, London, Special Publications*, *363*(1), 303–330. https://doi.org/10.1144/SP363.14

Anka, Z., Séranne, M., Lopez, M., Scheck-Wenderoth, M., & Savoye, B. (2009). The long-term evolution of the Congo deep-sea fan: A basin-wide view of the interaction between a giant submarine fan and a mature passive margin (ZaiAngo project). *Tectonophysics*, *470*(1), 42–56. https://doi.org/10.1016/j.tecto.2008.04.009

Aslanian, D., Moulin, M., Olivet, J.-L., Unternehr, P., Matias, L., Bache, F., et al. (2009). Brazilian and African passive margins of the central segment of the South Atlantic Ocean: Kinematic constraints. *Tectonophysics*, *468*(1), 98–112. https://doi.org/10.1016/j.tecto.2008.12.016

Asmus, H. E., & Ponte, F. C. (1973). The Brazilian marginal basins. In A. E. M. Nairn & F. G. Stehli (Eds.), *The South Atlantic* (pp. 87–133). Springer US. https://doi.org/10.1007/978-1-4684-3030-1_3

Athy, L. F. (1930). Density, porosity, and compaction of sedimentary rocks. *AAPG Bulletin*, *14*, 1–24. https://doi.org/10.1306/3D93289E-16B1-11D7-864500010

Azevedo, R., Antunes, R., & Bruni, M. (2022). Issues in the identification of the Aptian/Albian boundary in South Atlantic basins and beyond. *Carnets de Géologie*, *23*(1), 1–42. https://doi.org/10.2110/carnets.2022.2301

Baksi, A. K. (2018). Paraná flood basalt volcanism primarily limited to 1Myr beginning at 135Ma: New 40Ar/39Ar ages for rocks from Rio Grande do Sul, and critical evaluation of published radiometric data. *Journal of Volcanology and Geothermal Research*, *355*, 66–77. https://doi.org/10.1016/j.jvolgeores.2017.02.016

Bate, R. H. (1999). Non-marine ostracod assemblages of the Pre-Salt rift basins of West Africa and their role in sequence stratigraphy. *Geological Society, London, Special Publications*, *153*(1), 283–292. https://doi.org/10.1144/GSL.SP.1999.153.01.17

Bate, R. H., Cameron, N. R., & Brandão, M. G. P. (2001). The Lower Cretaceous (Pre-Salt) lithostratigraphy of the Kwanza basin, Angola. *Newsletters on Stratigraphy*, *38*(2–3), 117–127. https://doi.org/10.1127/nos/38/2001/117

Beaumont, C., & Ings, S. J. (2012). Effect of depleted continental lithosphere counterflow and inherited crustal weakness on rifting of the continental lithosphere: General results. *Journal of Geophysical Research*, *117*(B8), B08407. https://doi.org/10.1029/2012JB009203

Begg, G., Griffin, W., Natapov, L., O'Reilly, S. Y., Grand, S., O'Neill, C., et al. (2009). The lithospheric architecture of Africa: Seismic tomography, mantle petrology, and tectonic evolution. *Geosphere*, *5*(1), 23–50. https://doi.org/10.1130/GES00179.1

Beglinger, S. E., Doust, H., & Cloetingh, S. (2012a). Relating petroleum system and play development to basin evolution: Brazilian South Atlantic margin. *Petroleum Geoscience*, *18*(3), 315–336. https://doi.org/10.1144/1354-079311-022

Beglinger, S. E., Doust, H., & Cloetingh, S. (2012b). Relating petroleum system and play development to basin evolution: West African South Atlantic basins. *Marine and Petroleum Geology*, *30*(1), 1–25. https://doi.org/10.1016/j.marpetgeo.2011.08.008

Behar, F., Delhaye-Prat, V., & Garel, S. (2021). Detrital input quantification in lacustrine petroleum systems: An example of the pre-salt source rocks from the Lower Congo basin (Congo). *The Depositional Record*, *7*(1), 147–171. https://doi.org/10.1002/dep2.131

Beniest, A., Koptev, A., & Burov, E. (2017). Numerical models for continental break-up: Implications for the South Atlantic. *Earth and Planetary Science Letters*, *461*, 176–189. https://doi.org/10.1016/j.epsl.2016.12.034

Bento dos Santos, T. M., Tassinari, C. C., & Fonseca, P. E. (2015). Diachronic collision, slab break-off and long-term high thermal flux in the Brasiliano–Pan-African orogeny: Implications for the geodynamic evolution of the Mantiqueira Province. *Precambrian Research*, *260*, 1–22. https://doi.org/10.1016/j.precamres.2014.12.018

Blaich, O. A., Faleide, J. I., & Tsikalas, F. (2011). Crustal breakup and continent-ocean transition at South Atlantic conjugate margins. *Journal of Geophysical Research*, *116*(B1), B01402. https://doi.org/10.1029/2010JB007686

Boutilier, R. R., & Keen, C. E. (1999). Small-scale convection and divergent plate boundaries. *Journal of Geophysical Research*, *104*(B4), 7389–7403. https://doi.org/10.1029/1998JB900076

Brognon, G. P., & Verrier, G. R. (1966). Oil and geology in Cuanza basin of Angola. *AAPG Bulletin*, *50*, 108–158. https://doi.org/10.1306/5D25B471-16C1-11D7-8645000102C1865D

Brownfield, M. E., & Charpentier, R. R. (2006). Geology and total petroleum systems of the West-Central Coastal province (7203), West Africa (Version 1.0 ed.; Report). https://doi.org/10.3133/b2207B

Brune, S., Heine, C., Clift, P. D., & Pérez-Gussinyé, M. (2017). Rifted margin architecture and crustal rheology: Reviewing Iberia-Newfoundland, central South Atlantic, and South China Sea. *Marine and Petroleum Geology*, *79*, 257–281. https://doi.org/10.1016/j.marpetgeo.2016.10.018

Brune, S., Williams, S. E., Butterworth, N. P., & Mueller, R. D. (2016). Abrupt plate accelerations shape rifted continental margins. *Nature*, *536*(7615), 201–204. https://doi.org/10.1038/nature18319

Buck, W. R. (1991). Modes of continental lithospheric extension. *Journal of Geophysical Research*, *96*(B12), 20161–20178. https://doi.org/10.1029/91JB01485

Burke, K., MacGregor, D. S., & Cameron, N. R. (2003). Africa's petroleum systems: Four tectonic 'Aces' in the past 600 million years. *Geological Society, London, Special Publications*, *207*(1), 21–60. https://doi.org/10.1144/GSL.SP.2003.207.3

Burke, K., & Sengör, A. (1988). Ten metre global sea-level change associated with South Atlantic Aptian salt deposition. *Marine Geology*, *83*(1), 309–312. https://doi.org/10.1016/0025-3227(88)90064-3

Burov, E., & Poliakov, A. (2001). Erosion and rheology controls on synrift and postrift evolution: Verifying old and new ideas using a fully coupled numerical model. *Journal of Geophysical Research*, *106*(B8), 16461–16481. https://doi.org/10.1029/2001JB000433

Burwood, R. (1999). Angola: Source rock control for Lower Congo Coastal and Kwanza basin petroleum systems. *Geological Society, London, Special Publications*, *153*(1), 181–194. https://doi.org/10.1144/GSL.SP.1999.153.01.12

Cainelli, C., & Mohriak, W. U. (1999). Some remarks on the evolution of sedimentary basins along the eastern Brazilian continental margin. *International Union of Geological Sciences*, *22*(3), 206–216. https://doi.org/10.18814/epiiugs/1999/v22i3/008

Campos, C. W. M., Ponte, F. C., & Miura, K. (1974). Geology of the Brazilian Continental Margin. In C. A. Burk & C. L. Drake (Eds.), *The geology of continental margins* (pp. 447–461). Springer Berlin Heidelberg. https://doi.org/10.1007/978-3-662-01141-6_32

Carlson, R. L., & Raskin, G. S. (1984). Density of the ocean crust. *Nature*, *311*(5986), 555–558. https://doi.org/10.1038/311555a0

Celli, N. L., Lebedev, S., Schaeffer, A. J., & Gaina, C. (2020a). African cratonic lithosphere carved by mantle plumes. *Nature Communications*, *11*(1), 92. https://doi.org/10.1038/s41467-019-13871-2

Celli, N. L., Lebedev, S., Schaeffer, A. J., Ravenna, M., & Gaina, C. (2020b). The upper mantle beneath the South Atlantic Ocean, South America and Africa from waveform tomography with massive data sets. *Geophysical Journal International*, *221*(1), 178–204. https://doi.org/10.1093/gji/ggz574

Ceraldi, T. S., & Green, D. (2017). Evolution of the South Atlantic lacustrine deposits in response to Early Cretaceous rifting, subsidence and lake hydrology. *Geological Society, London, Special Publications*, *438*(1), 77–98. https://doi.org/10.1144/SP438.10

Chaboureau, A.-C., Donnadieu, Y., Sepulchre, P., Robin, C., Guillocheau, F., & Rohais, S. (2012). The Aptian evaporites of the South Atlantic: A climatic paradox? *Climate of the Past*, *8*(3), 1047–1058. https://doi.org/10.5194/cp-8-1047-2012

Chaboureau, A.-C., Guillocheau, F., Robin, C., Rohais, S., Moulin, M., & Aslanian, D. (2013). Paleogeographic evolution of the central segment of the South Atlantic during Early Cretaceous times: Paleotopographic and geodynamic implications. *Tectonophysics*, *604*(SI), 191–223. https://doi.org/10.1016/j.tecto.2012.08.025

Christeson, G. L., Goff, J. A., & Reece, R. S. (2019). Synthesis of oceanic crustal structure from two-dimensional seismic profiles. *Reviews of Geophysics*, *57*(2), 504–529. https://doi.org/10.1029/2019RG000641

Clerc, C., Ringenbach, J.-C., Jolivet, L., & Ballard, J.-F. (2017). Rifted margins: Ductile deformation, boudinage, continentward-dipping normal faults and the role of the weak lower crust. *Gondwana Research*, *53*, 20–40. https://doi.org/10.1016/j.gr.2017.04.030

Cohen, K. M., Finney, S. C., Gibbard, P. L., & Fan, J. X. (2013). The ICS International Chronostratigraphic Chart. *International Union of Geological Sciences*, *36*(3), 199–204. https://doi.org/10.18814/epiiugs/2013/v36i3/002

Cohen, K. M., Harper, D. A. T., & Gibbard, P. L. (2023). ICS International Chronostratigraphic Chart 2023/06. International Commission on Stratigraphy, IUGS. Retrieved from http://www.stratigraphy.org

Contrucci, I., Matias, L., Moulin, M., Geli, L., Klingelhofer, F., Nouze, H., et al. (2004). Deep structure of the West African continental margin (Congo, Zaire, Angola), between 5 degrees S and 8 degrees S, from reflection/refraction seismics and gravity data. *Geophysical Journal International*, *158*(2), 529–553. https://doi.org/10.1111/j.1365-246X.2004.02303.x

Coward, M. P., Purdy, E. G., Ries, A. C., & Smith, D. G. (1999). The distribution of petroleum reserves in basins of the South Atlantic margins. *Geological Society, London, Special Publications*, *153*(1), 101–131. https://doi.org/10.1144/GSL.SP.1999.153.01.08

Cowie, L., Angelo, R. M., Kusznir, N. J., Manatschal, G., & Horn, B. (2016). The palaeo-bathymetry of base Aptian salt deposition on the northern Angolan rifted margin: Constraints from flexural back-stripping and reverse post-break-up thermal subsidence modelling. *Petroleum Geoscience*, *22*(1), 59–70. https://doi.org/10.1144/petgeo2014-087

Crosby, A. G., White, N. J., Edwards, G. R. H., Thompson, M., Corfield, R., & Mackay, L. (2011). Evolution of deep-water rifted margins: Testing depth-dependent extensional models. *Tectonics*, *30*(1), TC1004. https://doi.org/10.1029/2010TC002687

Cui, X., Wignall, B., Freeman, K. H., & Summons, R. E. (2023). Early Cretaceous marine incursions into South Atlantic rift basins originated from the south. *Communications Earth & Environment*, *4*(1), 6. https://doi.org/10.1038/s43247-022-00668-3

Davis, M., & Kusznir, N. (2004). *4. Depth-dependent lithospheric stretching at rifted continental margins* (pp. 92–137). Columbia University Press. https://doi.org/10.7312/karn12738-005

Davison, I., Anderson, L., & Nuttall, P. (2012). Salt deposition, loading and gravity drainage in the Campos and Santos salt basins. *Geological Society, London, Special Publications*, *363*(1), 159–174. https://doi.org/10.1144/SP363.8

Delhaye-Prat, V., Dupont, G., Buratti, N., Moron, J., Esnault, J., Perrichot, V., et al. (2016). The Vembo Shales (Republic of the Congo): New insights on the transition from lacustrine to marine settings in the South Atlantic. Paper Number: 2850, T28.15.

de Ruiter, P. A. C. (1979). The Gabon and Congo basins salt deposits. *Economic Geology*, *74*(2), 419–431. https://doi.org/10.2113/gsecongeo.74.2.419

Dingle, R. V. (1996). Cretaceous Ostracoda of the SE Atlantic and SW Indian Ocean: A stratigraphical review and atlas. *Bulletin - Centres de Recherches Exploration-Production Elf- Aquitaine*, *16*, 1–17.

Dingle, R. V. (1999). Walvis Ridge barrier: Its influence on palaeoenvironments and source rock generation deduced from ostracod distributions in the early South Atlantic Ocean. *Geological Society, London, Special Publications*, *153*(1), 293–302. https://doi.org/10.1144/GSL.SP.1999.153.01.18

Dupre, S., Bertotti, G., & Cloetingh, S. (2007). Tectonic history along the South Gabon basin: Anomalous early post-rift subsidence. *Marine and Petroleum Geology*, *24*(3), 151–172. https://doi.org/10.1016/j.marpetgeo.2006.11.003

Eldrett, J. S., Bergman, S. C., Heine, C., Edwards, P., Jakeman, M., Miles, N., et al. (2023). Integrated bio- and chemo-stratigraphy for Early Cretaceous strata offshore Gabon: Additional constraints on the timing of salt deposition and rifting of the South Atlantic. *Marine and Petroleum Geology*, *148*, 106037. https://doi.org/10.1016/j.marpetgeo.2022.106037

Epin, M.-E., Manatschal, G., Sapin, F., & Rowan, M. G. (2021). The tectono-magmatic and subsidence evolution during lithospheric breakup in a salt-rich rifted margin: Insights from a 3D seismic survey from southern Gabon. *Marine and Petroleum Geology*, *128*, 105005. https://doi.org/10.1016/j.marpetgeo.2021.105005

Fernandez, O., Olaiz, A., Cascone, L., Hernandez, P., Pereira, A. D. F., Tritlla, J., et al. (2020). Geophysical evidence for breakup volcanism in the Angola and Gabon passive margins. *Marine and Petroleum Geology*, *116*, 104330. https://doi.org/10.1016/j.marpetgeo.2020.104330

Fossen, H., Cavalcante, C., Konopásek, J., Meira, V. T., de Almeida, R. P., Hollanda, M. H. B., & Trompette, R. (2020). A critical discussion of the subduction-collision model for the Neoproterozoic Araçuaí-West Congo orogen. *Precambrian Research*, *343*, 105715. https://doi.org/10.1016/j.precamres.2020.105715

Foulger, G. R. (2018). Origin of the South Atlantic igneous province. *Journal of Volcanology and Geothermal Research*, *355*, 2–20. https://doi.org/10.1016/j.jvolgeores.2017.09.004

Fullsack, P. (1995). An arbitrary Lagrangian-Eulerian formulation for creeping flows and its application in tectonic models. *Geophysical Journal International*, *120*(1), 1–23. https://doi.org/10.1111/j.1365-246X.1995.tb05908.x

Gindre-Chanu, L., Edoardo, P., Ian, S. R., Peacock, D., Roger, S., Ragnar, P., et al. (2016). Origin and diagenetic evolution of gypsum and microbialitic carbonates in the Late Sag of the Namibe basin (SW Angola). *Sedimentary Geology*, *342*, 133–153. https://doi.org/10.1016/j.sedgeo.2016.06.015

Gindre-Chanu, L., Pichat, A., Delhaye-Prat, V., Vis, C., Ringenbach, R., & Schlund, J.-M. (2022). Depositional and diagenetic model of the Aptian potash-bearing Loémé evaporites in onshore Congo. *Sedimentary Geology*, *427*, 106038. https://doi.org/10.1016/j.sedgeo.2021.106038

Gleason, G. C., & Tullis, J. (1995). A flow law for dislocation creep of quartz aggregates determined with the molten salt cell. *Tectonophysics*, *247*(1–4), 1–23. https://doi.org/10.1016/0040-1951(95)00011-B

Gordon, A. C., Mohriak, W. U., & Barbosa, V. C. F. (2013). Crustal architecture of the Almada basin, NE Brazil: An example of a non-volcanic rift segment of the South Atlantic passive margin. In *Conjugate divergent margins*. Geological Society of London. https://doi.org/10.1144/SP369.1

Graça, M. C., Kusznir, N., & Gomes Stanton, N. S. (2019). Crustal thickness mapping of the central South Atlantic and the geodynamic development of the Rio Grande Rise and Walvis Ridge. *Marine and Petroleum Geology*, *101*, 230–242. https://doi.org/10.1016/j.marpetgeo.2018.12.011

Griffin, W. L., O'Reilly, S. Y., Afonso, J. C., & Begg, G. C. (2008). The composition and evolution of lithospheric mantle: A re-evaluation and its tectonic implications. *Journal of Petrology*, *50*(7), 1185–1204. https://doi.org/10.1093/petrology/egn033

Griffin, W. L., O'Reilly, S. Y., & Ryan, C. G. (1999). The composition and origin of sub-continental lithospheric mantle. In *Mantle petrology: Field observations and high pressure experimentation: A tribute to Francis R. (Joe) Boyd* (Vol. 6, pp. 13–45). Geochem. Soc. Spec. Publ. https://doi.org/10.7312/karn12738-005

Guiraud, M., Buta-Neto, A., & Quesne, D. (2010). Segmentation and differential post-rift uplift at the Angola margin as recorded by the transform-rifted Benguela and oblique-to-orthogonal-rifted Kwanza basins. *Marine and Petroleum Geology*, *27*(5), 1040–1068. https://doi.org/10.1016/j.marpetgeo.2010.01.017

Guiraud, R., & Maurin, J. C. (1991). Le Rifting en Afrique au Cretace inferieur; synthese structurale, mise en evidence de deux etapes dans la genese des bassins, relations avec les ouvertures oceaniques peri-Africaines. *Bulletin de la Société Géologique de France*, *162*(5), 811–823. https://doi.org/10.2113/gssgfbull.162.5.811

Heine, C., Zoethout, J., & Mueller, R. D. (2013). Kinematics of the South Atlantic rift. *Solid Earth*, *4*(2), 215–253. https://doi.org/10.5194/se-4-215-2013

Hsü, K. (1972). Origin of saline giants: A critical review after the discovery of the Mediterranean evaporite. *Earth-Science Reviews*, *8*(4), 371–396. https://doi.org/10.1016/0012-8252(72)90062-1

Huismans, R. S., & Beaumont, C. (2008). Complex rifted continental margins explained by dynamical models of depth-dependent lithospheric extension. *Geology*, *36*(2), 163. https://doi.org/10.1130/G24231A.1

Huismans, R. S., & Beaumont, C. (2011). Depth-dependent extension, two-stage breakup and cratonic underplating at rifted margins. *Nature*, *473*(7345), 74–85. https://doi.org/10.1038/nature09988

Huismans, R. S., & Beaumont, C. (2014). Rifted continental margins: The case for depth-dependent extension. *Earth and Planetary Science Letters*, *407*(0), 148–162. https://doi.org/10.1016/j.epsl.2014.09.032

Jackson, M., Cramez, C., & Fonck, J. (2000). Role of subaerial volcanic rocks and mantle plumes in creation of South Atlantic margins: Implications for salt tectonics and source rocks. *Marine and Petroleum Geology*, *17*(4), 477–498. https://doi.org/10.1016/S0264-8172(00)00006-4

Karato, S.-I., & Wu, P. (1993). Rheology of the Upper Mantle: A synthesis. *Science*, *260*(5109), 771–778. https://doi.org/10.1126/science.260.5109.771

Karner, G. D., & Driscoll, N. W. (1999). Tectonic and stratigraphic development of the West African and eastern Brazilian Margins: Insights from quantitative basin modelling. *Geological Society, London, Special Publications*, *153*(1), 11–40. https://doi.org/10.1144/GSL.SP.1999.153.01.02

Karner, G. D., Driscoll, N. W., & Barker, D. H. N. (2003). Syn-rift regional subsidence across the West African continental margin: The role of lower plate ductile extension. *Geological Society, London, Special Publications*, *207*(1), 105–129. https://doi.org/10.1144/GSL.SP.2003.207.6

Karner, G. D., & Gambôa, L. A. P. (2007). Timing and origin of the South Atlantic pre-salt sag basins and their capping evaporites. *Geological Society, London, Special Publications*, *285*(1), 15–35. https://doi.org/10.1144/SP285.2

Kebi-Tsoumou, S. P. C. (2018). La phase d'hyperextension (sag) du rift de l'océan atlantique sud au congo: Milieux de dépôt, provenance des sédiments et paléoreliefs (Unpublished doctoral dissertation). University of Rennes 1.

Konstantinou, A., Karner, G. D., Kneller, E., & Gombosi, D. (2023). Salt deposition in ultradeep brine settings by dynamic inflow and evaporation. *AAPG Bulletin*, *107*(12), 2023–2052. https://doi.org/10.1306/05302322105

Kukla, P. A., Strozyk, F., & Mohriak, W. U. (2018). South Atlantic salt basins – Witnesses of complex passive margin evolution. *Gondwana Research*, *53*, 41–57. https://doi.org/10.1016/j.gr.2017.03.012

Lamb, S., Moore, J. D. P., Perez-Gussinye, M., & Stern, T. (2020). Global whole lithosphere isostasy: Implications for surface elevations, structure, strength, and densities of the continental lithosphere. *Geochemistry, Geophysics, Geosystems*, *21*(10), e2020GC009150. https://doi.org/10.1029/2020GC009150

Laspatzis, S., Rouby, D., Rohais, S., & Nardin, E. (2022). Meta-analysis of the long-term stratigraphic evolution of rifted margin basins: The GeoDyNamical Analysis approach applied to the South Atlantic Ocean. *Basin Research*, *n/a*(n/a), 1–34. https://doi.org/10.1111/bre.12740

Lavier, L., Ball, P. J., Manatschal, G., Heumann, M. J., MacDonald, J., Matt, V. J., & Schneider, C. (2019). Controls on the thermomechanical evolution of hyperextended lithosphere at magma-poor rifted margins: The example of Espirito Santo and the Kwanza basins. *Geochemistry, Geophysics, Geosystems*, *20*(11), 5148–5176. https://doi.org/10.1029/2019GC008580

Lawson, M., Sitgreaves, J., Rasbury, T., Wooton, K., Esch, W., Marcon, V., et al. (2022). New age and lake chemistry constraints on the Aptian pre-salt carbonates of the central South Atlantic. *GSA Bulletin*, *135*(3–4), 595–607. https://doi.org/10.1130/B36378.1

Lehner, P., & De Ruiter, P. A. C. (1977). Structural history of Atlantic Margin of Africa1. *AAPG Bulletin*, *61*(7), 961–981. https://doi.org/10.1306/C1EA43B0-16C9-11D7-8645000102C1865D

Lentini, M. R., Fraser, S. I., Sumner, H. S., & Davies, R. J. (2010). Geodynamics of the central South Atlantic conjugate margins: Implications for hydrocarbon potential. *Petroleum Geoscience*, *16*(3), 217–229. https://doi.org/10.1144/1354-079309-909

Louden, K., Osler, J., Srivastava, S., & Keen, C. (1996). Formation of oceanic crust at slow spreading rates: New constraints from an extinct spreading center in the Labrador Sea. *Geology*, *24*(9), 771–774. https://doi.org/10.1130/0091-7613(1996)024(0771:FOOCAS)2.3.CO;2

Loureiro, A., Schnürle, P., Klingelhöfer, F., Afilhado, A., Pinheiro, J., Evain, M., et al. (2018). Imaging exhumed lower continental crust in the distal Jequitinhonha basin, Brazil. *Journal of South American Earth Sciences*, *84*, 351–372. https://doi.org/10.1016/j.jsames.2018.01.009

Lu, G., & Huismans, R. S. (2021). Melt volume at Atlantic volcanic rifted margins controlled by depth-dependent extension and mantle temperature. *Nature Communications*, *12*(1), 3894. https://doi.org/10.1038/s41467-021-23981-5

Lu, G., & Huismans, R. S. (2022). Magmatism at passive margins: Effects of depth-dependent wide rifting and lithospheric counterflow. *Journal of Geophysical Research: Solid Earth*, *127*(3), e2021JB023046. https://doi.org/10.1029/2021JB023046

Marsh, J., & Swart, R. (2018). The Bero Volcanic Complex: Extension of the Paraná-Etendeka Igneous Province into SW Angola. *Journal of Volcanology and Geothermal Research*, *355*, 21–31. https://doi.org/10.1016/j.jvolgeores.2016.10.011

Marton, G. L., Tari, G. C., & Lehmann, C. T. (2000). Evolution of the Angolan Passive Margin, West Africa, with emphasis on post-salt structural styles. In *Atlantic rifts and continental margins* (pp. 129–149). American Geophysical Union (AGU). https://doi.org/10.1029/GM115p0129

Marzoli, A., Melluso, L., Morra, V., Renne, P., Sgrosso, I., D'Antonio, M., et al. (1999). Geochronology and petrology of Cretaceous basaltic magmatism in the Kwanza basin (western Angola), and relationships with the Paranà-Etendeka continental flood basalt province. *Journal of Geodynamics*, *28*(4), 341–356. https://doi.org/10.1016/S0264-3707(99)00014-9

Matthews, K. J., Maloney, K. T., Zahirovic, S., Williams, S. E., Seton, M., & Müller, R. D. (2016). Global plate boundary evolution and kinematics since the late Paleozoic. *Global and Planetary Change*, *146*, 226–250. https://doi.org/10.1016/j.gloplacha.2016.10.002

McKenzie, D. (1978). Some remarks on the development of sedimentary basins. *Earth and Planetary Science Letters*, *40*(1), 25–32. https://doi.org/10.1016/0012-821X(78)90071-7

McKenzie, D., & Bickle, M. J. (1988). The volume and composition of melt generated by extension of the lithosphere. *Journal of Petrology*, *29*(3), 625–679. https://doi.org/10.1093/petrology/29.3.625

Mitchell, N. C., Shi, W., Izzeldin, A., & Stewart, I. C. F. (2021). Reconstructing the level of the central Red Sea evaporites at the end of the Miocene. *Basin Research*, *33*(2), 1266–1292. https://doi.org/10.1111/bre.12513

Mohriak, W. U. (2020). Genesis and evolution of the South Atlantic volcanic islands offshore Brazil. *Geo-Marine Letters*, *40*(1), 1–33. https://doi.org/10.1007/s00367-019-00631-w

Montaron, B., & Tapponier, P. (2010). A quantitative model for salt deposition in actively spreading basins. Rio de Janeiro November 2009: Search and Discovery, Article 30117.

Moragas, M., Baqués, V., Martín-Martín, J. D., Sharp, I., Lapponi, F., Hunt, D., et al. (2023). Paleoenvironmental and diagenetic evolution of the Aptian Pre-Salt succession in Namibe basin (Onshore Angola). *Marine and Petroleum Geology*, *150*, 106153. https://doi.org/10.1016/j.marpetgeo.2023.106153

Morgan, W. J. (1983). Hotspot tracks and the early rifting of the Atlantic. *Tectonophysics*, *94*(1), 123–139. https://doi.org/10.1016/0040-1951(83)90013-6

Moulin, M., Aslanian, D., Olivet, J., Contrucci, I., Matias, L., Geli, L., et al. (2005). Geological constraints on the evolution of the Angolan margin based on reflection and refraction seismic data (ZaiAngo project). *Geophysical Journal International*, *162*(3), 793–810. https://doi.org/10.1111/j.1365-246X.2005.02668.x

Moulin, M., Aslanian, D., & Unternehr, P. (2010). A new starting point for the South and Equatorial Atlantic Ocean. *Earth-Science Reviews*, *98*(1–2), 1–37. https://doi.org/10.1016/j.earscirev.2009.08.001

Mueller, R. D., Seton, M., Zahirovic, S., Williams, S. E., Matthews, K. J., Wright, N. M., et al. (2016). Ocean basin evolution and global-scale plate reorganization events since Pangea breakup. In R. Jeanloz & K. H. Freeman (Eds.). *Annual Review of Earth and Planetary Sciences*, *44*(1), 107–138. ANNUAL REVIEWS. https://doi.org/10.1146/annurev-earth-060115-012211

Müller, R. D., Cannon, J., Qin, X., Watson, R. J., Gurnis, M., Williams, S., et al. (2018). GPlates: Building a virtual earth through deep time. *Geochemistry, Geophysics, Geosystems*, *19*(7), 2243–2261. https://doi.org/10.1029/2018GC007584

Nielsen, T. K., & Hopper, J. R. (2004). From rift to drift: Mantle melting during continental breakup. *Geochemistry, Geophysics, Geosystems*, *5*(7), Q07003. https://doi.org/10.1029/2003GC000662

Norton, I. O., Carruthers, D. T., & Hudec, M. R. (2016). Rift to drift transition in the South Atlantic salt basins: A new flavor of oceanic crust. *Geology*, *44*(1), 55–58. https://doi.org/10.1130/G37265.1

Nunn, J. A., & Harris, N. B. (2007). Subsurface seepage of seawater across a barrier: A source of water and salt to peripheral salt basins. *GSA Bulletin*, *119*(9–10), 1201–1217. https://doi.org/10.1130/B26088.1

Pedrosa-Soares, A. C., Alkmim, F. F., Tack, L., Noce, C. M., Babinski, M., Silva, L. C., & Martins-Neto, M. A. (2008). Similarities and differences between the Brazilian and African counterparts of the Neoproterozoic Araçuaí-west Congo orogen. *Geological Society, London, Special Publications*, *294*(1), 153–172. https://doi.org/10.1144/SP294.9

Pérez-Gussinyé, M., Andrés-Martínez, M., Araújo, M., Xin, Y., Armitage, J., & Morgan, J. P. (2020). Lithospheric strength and rift migration controls on synrift stratigraphy and breakup unconformities at rifted margins: Examples from numerical models, the Atlantic and South China Sea Margins. *Tectonics*, *39*(12), e2020TC006255. https://doi.org/10.1029/2020TC006255

Péron-Pinvidic, G., Manatschal, G., Masini, E., Sutra, E., Flament, J. M., Haupert, I., & Unternehr, P. (2015). Unravelling the along-strike variability of the Angola–Gabon rifted margin: A mapping approach. In *Petroleum geoscience of the West Africa Margin*. Geological Society of London. https://doi.org/10.1144/SP438

Pichel, L. M., Legeay, E., Ringenbach, J.-C., & Callot, J.-P. (2023). The West African salt-bearing rifted margin—Regional structural variability and salt tectonics between Gabon and Namibe. *Basin Research*, *n/a*(n/a), 1–32. https://doi.org/10.1111/bre.12796

Pindell, J., Graham, R., & Horn, B. (2014). Rapid outer marginal collapse at the rift to drift transition of passive margin evolution, with a Gulf of Mexico case study. *Basin Research*, *26*(6), 701–725. https://doi.org/10.1111/bre.12059

Pindell, J., & Heyn, T. (2022). Dynamo-thermal subsidence and sag–salt section deposition as magma-rich rifted margins move off plume centres along incipient lines of break-up. *Journal of the Geological Society*, *179*(5), jgs2021-095. https://doi.org/10.1144/jgs2021-095

Poropat, S. F., & Colin, J.-P. (2012). Early Cretaceous ostracod biostratigraphy of eastern Brazil and western Africa: An overview. *Gondwana Research*, *22*(3), 772–798. https://doi.org/10.1016/j.gr.2012.06.002

Quirk, D. G., Hertle, M., Jeppesen, J. W., Raven, M., Mohriak, W. U., Kann, D. J., et al. (2013). Rifting, subsidence and continental break-up above a mantle plume in the central South Atlantic. *Geological Society, London, Special Publications*, *369*(1), 185–214. https://doi.org/10.1144/SP369.20

Quirk, D. G., & Ruepke, L. H. (2018). Melt-induced buoyancy may explain the elevated rift-rapid sag paradox during breakup of continental plates. *Scientific Reports*, *8*(1), 9985. https://doi.org/10.1038/s41598-018-27981-2

Rebelo, T. B., Batezelli, A., & Luna, J. S. (2021). Stratigraphic evolution and carbonate factory implications: Case study of the Albian carbonates of the Campos basin, Brazil. *The Depositional Record*, *7*(2), 271–293. https://doi.org/10.1002/dep2.118

Reston, T. J. (2009). The extension discrepancy and syn-rift subsidence deficit at rifted margins. *Petroleum Geoscience*, *15*(3), 217–237. https://doi.org/10.1144/1354-079309-845

Reston, T. J. (2010). The opening of the central segment of the South Atlantic: Symmetry and the extension discrepancy. *Petroleum Geoscience*, *16*(3), 199–206. https://doi.org/10.1144/1354-079309-907

Rodriguez, C. R., Jackson, C. A.-L., Rotevatn, A., Bell, R. E., & Francis, M. (2018). Dual tectonic-climatic controls on salt giant deposition in the Santos basin, offshore Brazil. *Geosphere*, *14*(1), 215–242. https://doi.org/10.1130/GES01434.1

Romito, S., & Mann, P. (2022). Crustal structure of the Camamu-Almada Margin along the Northeastern Rift segment of Brazil from an integration of deep-penetration seismic reflection profiles, refraction, and gravity modeling. *Tectonics*, *41*(9), e2021TC007157. https://doi.org/10.1029/2021TC007157

Rowan, M. G. (2014). Passive-margin salt basins: Hyperextension, evaporite deposition, and salt tectonics. *Basin Research*, *26*(1), 154–182. https://doi.org/10.1111/bre.12043

Rowan, M. G. (2022). The ocean-continent transition of late synrift salt basins: Extension and evaporite deposition in the southern Gulf of Mexico and global analogs. In *From the Guajira Desert to the Apennines, and from Mediterranean Microplates to the Mexican Killer Asteroid: Honoring the Career of Walter Alvarez*. Geological Society of America. https://doi.org/10.1130/2022.2557(12)

Royden, L., & Keen, C. (1980). Rifting process and thermal evolution of the continental margin of Eastern Canada determined from subsidence curves. *Earth and Planetary Science Letters*, *51*(2), 343–361. https://doi.org/10.1016/0012-821X(80)90216-2

Salazar-Mora, C. A., Huismans, R. S., Fossen, H., & Egydio-Silva, M. (2018). The Wilson cycle and effects of tectonic structural inheritance on rifted passive margin formation. *Tectonics*, *37*(9), 3085–3101. https://doi.org/10.1029/2018TC004962

Saller, A., Rushton, S., Buambua, L., Inman, K., McNeil, R., & Dickson, J. A. D. T. (2016). Presalt stratigraphy and depositional systems in the Kwanza basin, offshore Angola. *AAPG Bulletin*, *100*(7), 1135–1164. https://doi.org/10.1306/02111615216

Sauter, D., Manatschal, G., Kusznir, N., Masquelet, C., Werner, P., Ulrich, M., et al. (2023). Ignition of the southern Atlantic seafloor spreading machine without hot-mantle booster. *Scientific Reports*, *13*(1), 1195. https://doi.org/10.1038/s41598-023-28364-y

Schmalz, R. F. (1969). Deep-water evaporite deposition: A genetic model1. *AAPG Bulletin*, *53*(4), 798–823. https://doi.org/10.1306/5D25C7FD-16C1-11D7-8645000102C1865D

Schutt, D. L., & Lesher, C. E. (2006). Effects of melt depletion on the density and seismic velocity of garnet and spinel lherzolite. *Journal of Geophysical Research*, *111*(B5), B05401. https://doi.org/10.1029/2003JB002950

Scott, D. R. (1992). Small-scale convection and mantle melting beneath mid-ocean ridges. *Washington DC American Geophysical Union Geophysical Monograph Series*, *71*, 327–352. https://doi.org/10.1029/GM071p0327

Séranne, M., & Anka, Z. (2005). South Atlantic continental margins of Africa: A comparison of the tectonic vs climate interplay on the evolution of equatorial West Africa and SW Africa margins. *Journal of African Earth Sciences*, *43*(1), 283–300. https://doi.org/10.1016/j.jafrearsci.2005.07.010

Seton, M., Müller, R., Zahirovic, S., Gaina, C., Torsvik, T., Shephard, G., et al. (2012). Global continental and ocean basin reconstructions since 200Ma. *Earth-Science Reviews*, *113*(3), 212–270. https://doi.org/10.1016/j.earscirev.2012.03.002

Simon, K., Huismans, R. S., & Beaumont, C. (2009). Dynamical modelling of lithospheric extension and small-scale convection: Implications for magmatism during the formation of volcanic rifted margins. *Geophysical Journal International*, *176*(1), 327–350. https://doi.org/10.1111/j.1365-246X.2008.03891.x

Simon, N. S., & Podladchikov, Y. Y. (2008). The effect of mantle composition on density in the extending lithosphere. *Earth and Planetary Science Letters*, *272*(1), 148–157. https://doi.org/10.1016/j.epsl.2008.04.027

Stanton, N., Kusznir, N., Gordon, A., & Schmitt, R. (2019). Architecture and tectono-magmatic evolution of the Campos rifted margin: Control of OCT structure by basement inheritance. *Marine and Petroleum Geology*, *100*, 43–59. https://doi.org/10.1016/j.marpetgeo.2018.10.043

Steckler, M., & Watts, A. (1978). Subsidence of the Atlantic-type continental margin off New York. *Earth and Planetary Science Letters*, *41*(1), 1–13. https://doi.org/10.1016/0012-821X(78)90036-5

Steinberger, B., & Becker, T. W. (2018). A comparison of lithospheric thickness models. *Tectonophysics*, *746*, 325–338. https://doi.org/10.1016/j.tecto.2016.08.001

Strozyk, F., Back, S., & Kukla, P. A. (2017). Comparison of the rift and post-rift architecture of conjugated salt and salt-free basins offshore Brazil and Angola/Namibia, South Atlantic. *Tectonophysics*, *716*, 204–224. https://doi.org/10.1016/j.tecto.2016.12.012

Svartman Dias, A. E., Lavier, L., & Hayman, N. W. (2015). Conjugate rifted margins width and asymmetry: The interplay between lithospheric strength and thermomechanical processes. *Journal of Geophysical Research: Solid Earth*, *120*(12), 8672–8700. https://doi.org/10.1002/2015JB012074

Szameitat, L. S. A., Heilbron, M., de Aragão, M. A. N. F., Manatschal, G., Ferreira, F. J. F., de Barros e Silva Bongiolo, A., et al. (2023). Geophysical evidence for lithospheric scale asymmetry and inherited mantle in the SE Brazilian-Angola and Newfoundland-Iberia rifted margins. *Journal of South American Earth Sciences*, *123*, 104214. https://doi.org/10.1016/j.jsames.2023.104214

Szatmari, P. (2000). Habitat of petroleum along South Atlantic margins. In *Petroleum systems of South Atlantic Margins*. American Association of Petroleum Geologists. https://doi.org/10.1306/M73705C6

Szatmari, P., & Milani, E. J. (2016). Tectonic control of the oil-rich large igneous-carbonate-salt province of the South Atlantic rift. *Marine and Petroleum Geology*, *77*, 567–596. https://doi.org/10.1016/j.marpetgeo.2016.06.004

Szatmari, P., Moré de Lima, C., Fontaneta, G., de Melo Lima, N., Zambonato, E., Menezes, M. R., et al. (2021). Petrography, geochemistry and origin of South Atlantic evaporites: The Brazilian side. *Marine and Petroleum Geology*, *127*, 104805. https://doi.org/10.1016/j.marpetgeo.2020.104805

Tappe, S., Smart, K., Torsvik, T., Massuyeau, M., & de Wit, M. (2018). Geodynamics of kimberlites on a cooling Earth: Clues to plate tectonic evolution and deep volatile cycles. *Earth and Planetary Science Letters*, *484*, 1–14. https://doi.org/10.1016/j.epsl.2017.12.013

Teisserenc, P., & Villemin, J. (1989). Sedimentary basin of Gabon—Geology and Oil Systems. In *Divergent/passive margin basins*. American Association of Petroleum Geologists. https://doi.org/10.1306/M48508C3

Tenzer, R., & Chen, W. (2019). Mantle and sub-lithosphere mantle gravity maps from the LITHO1.0 global lithospheric model. *Earth-Science Reviews*, *194*, 38–56. https://doi.org/10.1016/j.earscirev.2019.05.001

Theunissen, T., & Huismans, R. S. (2019). Long-term coupling and feedback between tectonics and surface processes during non-volcanic rifted margin formation. *Journal of Geophysical Research: Solid Earth*, *124*(11), 12323–12347. https://doi.org/10.1029/2018JB017235

Theunissen, T., & Huismans, R. S. (2022). Mantle exhumation at magma-poor rifted margins controlled by frictional shear zones. *Nature Communications*, *13*(1), 1634. https://doi.org/10.1038/s41467-022-29058-1

Theunissen, T., Huismans, R. S., Lu, G., & Riel, N. (2022). Relative continent - Mid-ocean ridge elevation: A reference case for isostasy in geodynamics. *Earth-Science Reviews*, *233*, 104153. https://doi.org/10.1016/j.earscirev.2022.104153

Theunissen, T., Huismans, R. S., Rouby, D., & Gout, C. (2024). 2-D geodynamic modelling of the central South Atlantic wide rifted margins, implications for evaporite deposition - Supplementary videos and data [Dataset]. FigShare. https://doi.org/10.6084/m9.figshare.24128562

Thieulot, C. (2011). FANTOM: Two- and three-dimensional numerical modelling of creeping flows for the solution of geological problems. *Physics of the Earth and Planetary Interiors*, *188*(1–2), 47–68. https://doi.org/10.1016/j.pepi.2011.06.011

Thompson, D. L., Stilwell, J. D., & Hall, M. (2015). Lacustrine carbonate reservoirs from Early Cretaceous rift lakes of Western Gondwana: Pre-Salt coquinas of Brazil and West Africa. *Gondwana Research*, *28*(1), 26–51. https://doi.org/10.1016/j.gr.2014.12.005

Torsvik, T. H., Rousse, S., Labails, C., & Smethurst, M. A. (2009). A new scheme for the opening of the South Atlantic Ocean and the dissection of an Aptian salt basin. *Geophysical Journal International*, *177*(3), 1315–1333. https://doi.org/10.1111/j.1365-246X.2009.04137.x

Tucker, M. E. (1991). Sequence stratigraphy of carbonate-evaporite basins: Models and application to the Upper Permian (Zechstein) of northeast England and adjoining North Sea. *Journal of the Geological Society*, *148*(6), 1019–1036. https://doi.org/10.1144/gsjgs.148.6.1019

Unternehr, P., Péron-Pinvidic, G., Manatschal, G., & Sutra, E. (2010). Hyper-extended crust in the South Atlantic: In search of a model. *Petroleum Geoscience*, *16*(3), 207–215. https://doi.org/10.1144/1354-079309-904

Van Eden, J. G. (1978). Stratiform copper and zinc mineralization in the Cretaceous of Angola. *Economic Geology*, *73*(6), 1154–1161. https://doi.org/10.2113/gsecongeo.73.6.1154

Warren, J. K. (2016). Evaporites a geological compendium.

Watts, A., & Ryan, W. (1976). Flexure of the lithosphere and continental margin basins. *Tectonophysics*, *36*(1), 25–44. https://doi.org/10.1016/0040-1951(76)90004-4

White, R. S., Minshull, T. A., Bickle, M. J., & Robinson, C. J. (2001). Melt generation at very slow-spreading oceanic ridges: Constraints from geochemical and geophysical data. *Journal of Petrology*, *42*(6), 1171–1196. https://doi.org/10.1093/petrology/42.6.1171

Wolf, S. G., Huismans, R. S., Braun, J., & Yuan, X. (2022). Topography of mountain belts controlled by rheology and surface processes. *Nature*, *606*(7914), 516–521. https://doi.org/10.1038/s41586-022-04700-6

Zalán, P. V., Severino, M. D. C. G., Rigoti, C. A., Magnavita, L. P., Oliveira, J. A. B., & Viana, A. R. (2011). An entirely new 3-D view of the crustal and mantle structure of a South Atlantic Passive Margin – Santos, Campos and Espírito Santo basins, Brazil. In *AAPG annual convention and exhibition*.

References From the Supporting Information

Artemieva, I. M. (2006). Global 1x1 thermal model TC1 for the continental lithosphere: Implications for lithosphere secular evolution. *Tectonophysics*, *416*(1), 245–277. https://doi.org/10.1016/j.tecto.2005.11.022

Asimow, P. D., Dixon, J. E., & Langmuir, C. H. (2004). A hydrous melting and fractionation model for mid-ocean ridge basalts: Application to the Mid-Atlantic Ridge near the Azores. *Geochemistry, Geophysics, Geosystems*, *5*(1), 2003GC000568. https://doi.org/10.1029/2003GC000568

Braun, M. G., Hirth, G., & Parmentier, E. (2000). The effects of deep damp melting on mantle flow and melt generation beneath mid-ocean ridges. *Earth and Planetary Science Letters*, *176*(3), 339–356. https://doi.org/10.1016/S0012-821X(00)00015-7

Chamot-Rooke, N., Gaulier, J.-M., & Jestin, F. (1999). Constraints on Moho depth and crustal thickness in the Liguro-Proven¸cal basin from a 3D gravity inversion: Geodynamic implications. *Geological Society, London, Special Publications*, *156*(1), 37–61. https://doi.org/10.1144/GSL.SP.1999.156.01.04

Choblet, G., & Parmentier, E. (2001). Mantle upwelling and melting beneath slow spreading centers: Effects of variable rheology and melt productivity. *Earth and Planetary Science Letters*, *184*(3), 589–604. https://doi.org/10.1016/S0012-821X(00)00330-7

Choi, E., Buck, W. R., Lavier, L., & Petersen, K. D. (2013). Using core complex geometry to constrain fault strength. *Geophysical Research Letters*, *40*(15), 3863–3867. https://doi.org/10.1002/grl.50732

Cowie, P., & Karner, G. D. (1990). Gravity effect of sediment compaction: Examples from the North Sea and the Rhine Graben. *Earth and Planetary Science Letters*, *99*(1–2), 141–153. https://doi.org/10.1016/0012-821X(90)90078-C

Goteti, R., Ings, S. J., & Beaumont, C. (2012). Development of salt minibasins initiated by sedimentary topographic relief. *Earth and Planetary Science Letters*, *339*, 103–116. https://doi.org/10.1016/j.epsl.2012.04.045

Guan, H., Geoffroy, L., & Xu, M. (2021). Magma-assisted fragmentation of Pangea: Continental breakup initiation and propagation. *Gondwana Research*, *96*, 56–75. https://doi.org/10.1016/j.gr.2021.04.003

Hirth, G., & Kohlstedt, D. L. (1996). Water in the oceanic upper mantle: Implications for rheology, melt extraction and the evolution of the lithosphere. *Earth and Planetary Science Letters*, *144*(1), 93–108. https://doi.org/10.1016/0012-821X(96)00154-9

Huismans, R. S., & Beaumont, C. (2002). Asymmetric lithospheric extension: The role of frictional plastic strain softening inferred from numerical experiments. *Geology*, *30*(3), 211–214. https://doi.org/10.1130/0091-7613(2002)030⟨0211:ALETRO⟩2.0.CO;2

Karato, S.-I. (1986). Does partial melting reduce the creep strength of the upper mantle? *Nature*, *319*(6051), 309–310. https://doi.org/10.1038/319309a0

Lavier, L., Buck, W. R., & Poliakov, A. N. B. (2000). Factors controlling normalfault offset in an ideal brittle layer. *Journal of Geophysical Research*, *105*(B10), 23431–23442. https://doi.org/10.1029/2000JB900108

Le Pichon, X., Jellinek, M., Lenardic, A., Şengör, A. M. C., & İmren, C. (2021). Pangea migration. *Tectonics*, *40*(6), e2020TC006585. https://doi.org/10.1029/2020TC006585

Le Pichon, X., Sengor, A. M. C., & Imren, C. (2019). Pangea and the lower mantle. *Tectonics*, *38*(10), 3479–3504. https://doi.org/10.1029/2018TC005445

Lenardic, A. (2017). A supercontinental boost. *Nature Geoscience*, *10*(1), 4–5. https://doi.org/10.1038/ngeo2862

Roberts, A., Kusznir, N., Yielding, G., & Styles, P. (1998). 2D flexural backstripping of extensional basins; the need for a sideways glance. *Petroleum Geoscience*, *4*, 327–338. https://doi.org/10.1144/petgeo.4.4.327

Tenzer, R., & Gladkikh, V. (2014). Assessment of density variations of marine sediments with ocean and sediment depths. *The Scientific World Journal*, *2014*, 9. Article ID 823296. https://doi.org/10.1155/2014/823296

Van Avendonk, H. J. A., Davis, J. K., Harding, J. L., & Lawver, L. A. (2017). Decrease in oceanic crustal thickness since the breakup of Pangaea. *Nature Geoscience*, *10*(1), 58–61. https://doi.org/10.1038/ngeo2849

van den Belt, F. J. G., & de Boer, P. L. (2007). A shallow-basin model for 'saline giants' based on isostasy-driven subsidence. In *Sedimentary processes, environments and basins* (pp. 241–252). John Wiley & Sons, Ltd. https://doi.org/10.1002/9781444304411.ch11